Technical Note: Nighttime OH and HO_2 chemical equilibria in the mesosphere – lower thermosphere

Mikhail Yu. Kulikov[1,2], Mikhail V. Belikovich[1,2], Aleksey G. Chubarov[1,2], Svetlana O. Dementyeva[1], and Alexander M. Feigin[1,2]

[1]A. V. Gaponov-Grekhov Institute of Applied Physics of the Russian Academy of Sciences, 46 Ulyanov Str., 603950 Nizhny Novgorod, Russia

[2]Lobachevsky State University of Nizhny Novgorod, 23 Gagarin Avenue, Nizhny Novgorod, Russia, 603022

Correspondence to: Mikhail Yu. Kulikov (mikhail_kulikov@mail.ru)

Abstract. At the altitudes of the mesosphere – lower thermosphere OH and HO_2 play a significant role in many physicochemical processes. Thus, monitoring their spatiotemporal evolution together with other chemically active trace gases is one of the most important problems for this atmosphere region, in which direct measurements are difficult. The paper studies the nighttime OH and HO_2 chemical equilibria using the 3D chemical transport modeling within the general approach, which includes the identification of the main sources and sinks in the equilibrium space-time areas and derivation of analytical criteria for equilibrium validity. The presented analysis shows, that there are extended areas, where nighttime HO_2 and OH are close to their local equilibrium concentrations, determined mainly by the reaction between HO_x – O_x components among themselves and with H_2O_2, N, NO, NO_2 and CO. In the upper mesosphere – lower thermosphere the equilibrium expressions can be shortened, so that they include the HO_x – O_x chemistry only. These expressions describe the HO_2 and OH equilibria from the top down to some boundaries, the altitude positions of which vary in the interval between 72-73 and 85 km and depend essentially on season and latitude. The developed analytical criteria almost everywhere reproduce well the main features of these boundaries. Due to weak sensitivity to uncertainties of reaction rates and other parameters, the criteria can be considered a robust instrument for HO_2 and OH equilibrium validation. The obtained results allow us to extend previously proposed methods for the retrieval of poorly measured components from measurement data and to develop new approaches.

1 Introduction

Monitoring the spatiotemporal evolution of chemically active trace gases is one of the most important problems in atmospheric research. Despite the increase of the experimental data volume nowadays, primarily due to the development in remote sensing methods, many important trace gases continue to be unavailable for direct and regular measurements. A well-known way to increase the information content of experimental campaigns is to use the available experimental data in conjunction with a certain chemical or physicochemical model to derive unmeasured characteristics indirectly. Within the framework of this approach, the model acts as *a priori* relationship between directly measured and retrieved characteristics. The simplest model, that makes it possible to implement this approach, is based on the condition of local (in both time and space) photochemical/chemical balance (local equilibrium) between sources and sinks of the so-called "fast" components: trace gases with short lifetimes relatively, in particular, to the characteristic transport times. Mathematically this condition does not mean that the fast variables are at equilibrium, but when it is fulfilled, the corresponding concentrations are close to their instantaneous equilibrium values. At the same time due to the strong dissipation in most cases (except the special cases where the ensemble of fast components includes the slow family of these components), there is no need to follow the law of matter conservation. It is possible to disregard insignificant sinks and sources, including those caused by transport, in the corresponding balance equations without the loss of accuracy. The resulting algebraic equations are the simplest *a priori* local relations between measurable and retrieved trace gases. These relationships can be used to derive information about hard-to-measure atmospheric species, determine key atmospheric characteristics (for example, temperature (Marchand et al., 2007)), validate the data quality of simultaneous measurements of several atmospheric components (Kulikov et al., 2018a), estimate reaction rate constants (Stedman et al., 1975; Avallone and Toohey, 2001), evaluate sources/sinks (Cantrell et al., 2003), etc.

For several decades the photochemical/chemical equilibrium approximation has been used to solve many atmospheric tasks. It is applied (see, e.g., the short review in Kulikov et al. (2018a) and references therein) in investigations of the surface layer and free troposphere chemistry in different regions (over megapolises, in rural areas, in the mountains, over the seas), in stratospheric chemistry studies, including derivation of critical parameters in the ozone destruction catalytic cycles, and in studies of the HO_x – O_x chemistry and airglows **(**$O(^1S)$ green-line, O_2 A-band, OH Meinel band emissions**)** at the heights of the mesosphere – lower thermosphere. In the latter case the distributions of unmeasured characteristics are determined from the data of daytime and nighttime rocket and satellite measurements (e.g., Evans and Llewellyn, 1973; Good, 1976; Pendleton et al., 1983; McDade et al., 1985; McDade and Llewellyn, 1988; Evans et al., 1988; Thomas, 1990; Llewellyn et al., 1993; Llewellyn and McDade, 1996; Russell and Lowe, 2003; Russell et al., 2005; Kulikov et al., 2006, 2009, 2017, 2022a, 2022b; Mlynczak et al., 2007,

2013a, 2013b, 2014, 2018; Smith et al., 2010; Xu et al., 2012; Siskind et al., 2008, 2015; Fytterer et al., 2019) with the use of equilibrium assumptions for ozone and excited states of OH, O, and O_2. For example, such an approach is applied to the data of the SABER (Sounding of the Atmosphere using Broadband Emission Radiometry) instrument onboard the TIMED (Thermosphere Ionosphere Mesosphere Energetics and Dynamics) satellite, which since 2002 continues to measure simultaneous profiles of temperature, ozone and volume emission rates of OH* transitions in wide ranges of altitude, local time and latitude with a rather high space-time resolution.

Note a number of general aspects of the application of equilibrium conditions in the above examples. First of all, there are no clear criteria, indicating the conditions under which the use of equilibrium approximation is justified. Usually a certain component is taken to be a fast variable, if its lifetime is much shorter, than the lifetimes of other components of studied photochemical/chemical system or the duration of a day, daytime, nighttime, etc. For example, in the papers on SABER data processing (Mlynczak et al., 2013a, 2013b, 2014, 2018) it is assumed, that the nighttime ozone chemical equilibrium in the mesopause is well fulfilled at altitudes of 80–100 km, since the nighttime ozone lifetime at these altitudes varies in the range from several minutes to several tens of minutes. Note, that this assumption is quite popular and used in different tasks (e.g., Swenson and Gardner, 1998; Marsh et al., 2006; Smith et al., 2009; Nikoukar et al., 2007; Xu et al., 2010, 2012; Kowalewski et al., 2014; Grygalashvyly et al., 2014; Grygalashvyly, 2015; Sonnemann et al., 2015; Kulikov et al., 2021). Belikovich et al. (2018) and Kulikov et al. (2018b, 2019, 2023a) analyzed the nighttime ozone chemical equilibrium numerically, analytically, and with the use of SABER/TIMED data. It was revealed, that the short lifetime is not a sufficient condition, so, this equilibrium may be significantly disturbed above 80 km. The local ratio between true and equilibrium concentrations may vary widely and reach up to several orders of magnitude (e.g., Figure 5 in Kulikov et al. (2018b)). Thus, without special restrictions the error in retrieved characteristics due to the use of equilibrium approximation is uncontrollable and may significantly exceed all other errors in the retrieval procedure due to, for example, uncertainties in the measurement data and rate constants.

Since the papers of Belikovich et al. (2018) and Kulikov et al. (2018b, 2019, 2023a), we developed the general approach to correctly identify fast components, employing the data from a global 3D chemical transport model. It includes:

1. Plotting of the equilibrium space-time maps of the components of interest.
2. Identification of the main sources and sinks in the found equilibrium areas.
3. Derivation and subsequent use of analytical criteria that make it possible to determine the fulfillment of the equilibrium condition locally (in time and space) with the use of the measurement data only.

The latter point is based on the theory of chemical equilibrium of a certain trace gas, acquired from estimations of its lifetime and equilibrium concentration, and time dependences of these characteristics (Kulikov et al., 2023a). Note, that when equilibrium condition is applied to measurement data in the retrieval of unmeasured characteristics, the criterion allows controlling and limiting the possible error caused by the equilibrium approximation.

The main goal of the paper is to apply this approach to the analysis of nighttime OH and HO_2 chemical equilibria in the mesosphere – lower thermosphere. Along with O and H, OH and HO_2 are important components of HO_x – O_x chemistry, participating (a) in chemical heating through, in particular, $O+OH \rightarrow O_2+H$ and $O+HO_2 \rightarrow O_2+OH$ exothermic reactions, (b) in formation of airglows, (c) in catalytic cycles of the ozone destruction. Moreover, the equilibrium conditions of OH and HO_2 are additional *a priori* relationships, that can be used to retrieve these components or other characteristics from measured data. In particular, Panka et al. (2021) proposed the method for nighttime total OH retrieval from SABER/TIMED data at 80-100 km, which does not use the ozone chemical equilibrium. However, the method applies the equilibrium between sources and sinks not only to excited states of OH with ultrashort lifetimes, but also to the ground state. Therefore, this point is verified in our paper.

In the next section we present the used model and methods. In Section 3 the model data are used to plot HO_2 and OH equilibrium maps. In Sections 4-5 we identify the main reactions, determining equilibria of these gases, and present their shortened equilibria conditions at the upper mesosphere and lower thermosphere altitudes. In Section 6 the criteria for HO_2 and OH equilibria validity are developed. In Section 7 we discuss the obtained results and their possible applications.

2 Used 3D model and Approaches

The analysis of OH and HO_2 nighttime chemical equilibria was carried out, using the data, obtained with calculation of 3D chemical transport model of the middle atmosphere, developed at the Leibniz Institute of Atmospheric Physics (e.g., Sonnemann et al., 1998; Körner & Sonnemann, 2001; Grygalashvyly et al., 2009; Hartogh et al., 2004, 2011) to investigate the mesosphere – lower thermosphere chemistry, in particular, in the extended mesopause region. A number of papers (e.g., Hartogh et al., 2004, 2011; Sonnemann, et al., 2006, 2008) validated the model with measurements, in particular, for ozone and water vapor.

The space-time distribution of temperature and winds were taken from the model of the dynamics of the middle atmosphere COMMA-IAP (e.g., Kremp et al., 1999; Berger and von Zahn, 1999) with an updated frequency of 1 day and linear smoothing between subsequent updates to avoid unrealistic jumps

in the calculated concentrations of trace gases. 3D advective transport is taken into account with the use of the Walcek-scheme (Walcek, 2000). The vertical diffusive transport (turbulent and molecular) is calculated with the use of the implicit Thomas algorithm (Morton and Mayers, 1994). The model grid has 118 pressure-height levels (0–135 km), 16 latitudinal and 32 longitudinal levels. The chemical module (see Table 1) comprises 25 constituents (O, O(^{1}D), O_3, H, OH, HO_2, H_2O_2, H_2O, H_2, N, NO, NO_2, NO_3, N_2O, CH_4, CH_2, CH_3, CH_3O_2, CH_3O, CH_2O, CHO, CO, CO_2, O_2, N_2), 54 chemical reactions between them and 15 photo-dissociation reactions. The model utilizes the pre-calculated dissociation rates (Kremp et al., 1999) and their dependence on the altitude and solar zenith angle.

The model was used to calculate a one-year global evolution of the above mentioned trace gases. To remove the transition regions corresponding to sunset and sunrise, we use only local times when the solar zenith angle $\chi > 105°$. As a result, we find the spatiotemporal series of the OH/OH^{eq} and $HO_2/{HO_2}^{eq}$ ratios. Here OH and HO_2 are the local nighttime values of hydroxyl and hydroperoxyl radicals, calculated by the model, OH^{eq} and ${HO_2}^{eq}$ are their local equilibrium values, corresponding to the instantaneous balance between production and loss terms respectively. To determine each local value of OH^{eq} and ${HO_2}^{eq}$ we used the local values of the parameters (temperature, O_2, and N_2) and the concentrations of other trace gases, determining local chemical sources and sinks of OH and HO_2. Then the OH/OH^{eq} and $HO_2/{HO_2}^{eq}$ series were averaged over the zonal coordinate and time during each month and were presented as height-latitude maps, depending on the month. Each map contains lines, marking the boundaries of the equilibrium areas, where the following conditions are satisfied:

$$\begin{cases} |< OH/OH^{eq} > -1| \le 0.1 \\ \sigma_{OH/OH^{eq}} \le 0.1 \end{cases}, \begin{cases} |< HO_2/{HO_2}^{eq} > -1| \le 0.1 \\ \sigma_{HO_2/{HO_2}^{eq}} \le 0.1 \end{cases}, \quad (1)$$

where the angle brackets are used to denote the values averaged in time and space, $\sigma_{OH/OH^{eq}}$ and $\sigma_{HO_2/{HO_2}^{eq}}$ are standard deviations of the OH/OH^{eq} and $HO_2/{HO_2}^{eq}$ ratios from 1 respectively.

Then we plotted spatiotemporal maps, showing the relative contribution of each reaction to a summarized source or sink at all altitudes and latitudes. These maps helped us to identify the main sources and sinks, describing the chemical equilibrium of nighttime OH and HO_2 in the equilibrium areas to an accuracy of better than a few percent.

Finally, we obtained and verified the analytical criteria of OH and HO_2 nighttime chemical equilibria according to Kulikov et al. (2023a). The paper considered the pure chemical evolution of a certain trace gas n:

$$\frac{dn}{dt} = I_n - S_n = -\frac{1}{\tau_n}(n - n^{eq}),$$

$$\tau_n = \frac{n}{S_n},\ n^{eq} = \frac{n \cdot I_n}{S_n}, \quad (2)$$

where t is time, I_n and S_n are total photochemical/chemical sources and sinks of n respectively, τ_n is the n lifetime and n^{eq} is its equilibrium concentration, corresponding to the condition $I_n = S_n$. The lifetime determines the characteristic time scale, for which n approaches n^{eq}, when $n^{eq} = const$. In general case τ_n and n^{eq} are functions of time. Kulikov et al. (2023a) showed strictly mathematically, that the local values of n and n^{eq} are close to each other ($n(t) \approx n^{eq}(t)$), when $\tau_n \ll \tau_{n^{eq}}$, where $\tau_{n^{eq}}$ is the local time scale of n^{eq}:

$$\tau_{n^{eq}} \equiv \frac{n^{eq}}{|dn^{eq}/dt|}. \quad (3)$$

The expression for τ_n is found from the total sink of n. The expression for $\tau_{n^{eq}}$ is derived from Eq. (3) with the use of differential equations, describing chemical evolution of other reacting components, which determine the expression for n^{eq}. Kulikov et al. (2023a) also showed, when $\tau_n \ll \tau_{n^{eq}}$, $n \cong n^{eq}(1 - sign(\frac{dn^{eq}}{dt}) \cdot \frac{\tau_n}{\tau_{n^{eq}}})$ in the first order approximation. Thus, the criterion

$$\tau_n/\tau_{n^{eq}} \leq 0.1 \quad (4)$$

is sufficient, in order to the possible relative difference between n and n^{eq} to be no more than 0.1.

3 Nighttime HO_2 and OH chemical equilibria

According to the Table 1 HO_2 chemical sources in nighttime are determined by the following reactions:

H+O_2+M → HO_2+M (R20), OH+O_3 → O_2+HO_2 (R22), H_2O_2+OH → H_2O+HO_2 (R29), H_2O_2+O → OH+HO_2 (R19), CHO+O_2 → HO_2+CO (R40), CH_3O+O_2 → CH_2O+HO_2 (R37),

whereas chemical sinks of this component are as follows:

HO_2+O → OH+O_2 (R18), HO_2+O_3 → OH+2O_2 (R23), OH+HO_2 → H_2O+O_2 (R28), H+HO_2 → 2OH (R14), H+HO_2 → H_2O+O (R15), H+HO_2 → H_2+O_2 (R16), NO+HO_2 → NO_2+OH (R50), HO_2+HO_2 → H_2O_2+O_2 (R30), HO_2+HO_2+M → H_2O_2+O_2+M (R31).

Thus, HO_2 local equilibrium concentration is described by the following equation:

$$HO_2{}^{eq} = \frac{k_{20} \cdot H \cdot M \cdot O_2 + k_{22} \cdot OH \cdot O_3 + k_{29} \cdot H_2O_2 \cdot OH + k_{19} \cdot H_2O_2 \cdot O + k_{40} \cdot CHO \cdot O_2 + k_{37} \cdot CH_3O \cdot O_2}{k_{18} \cdot O + k_{23} \cdot O_3 + k_{28} \cdot OH + (k_{14} + k_{15} + k_{16}) \cdot H + k_{50} \cdot NO + 2 \cdot (k_{30} + k_{31} \cdot M) \cdot HO_2} \quad (5)$$

Figure 1 plots height-latitude cross sections for the $< HO_2/HO_2{}^{eq} >$ ratio for each month. The black solid lines mark the boundaries of equilibrium areas, where according to condition (1) local values of HO_2 are close to their equilibrium values with a possible bias of less than 10%. At low and middle latitudes one can see the presence of the main equilibrium area, which extends from the top of the analyzed altitude range to the lower boundary. The height of this equilibrium boundary, $z_{HO_2^{eq}}$, depends on the season and latitude and varies in the interval between 73 and 85 km. It is the highest and the lowest during the summer and winter respectively at the middle latitudes. Near the equator $z_{HO_2^{eq}}$ demonstrates the weakest annual variations and varies in the 81-83 km range. There are local areas below the upper longest black line, but they are small and irregular and can be omitted from our consideration. Note that the maps show the existence of equilibrium near 50 km, which can be assumed to be the beginning of the main equilibrium area in the stratosphere. At high latitudes there is the main equilibrium area as at low and middle latitudes, but this area above 70-75° of latitude can extend down to 50 km.

In accordance to the Table 1 OH chemical sources are determined by the following reactions:

$H+O_3 \rightarrow OH+O_2$ (R21), $HO_2+O \rightarrow OH+O_2$ (R18), $HO_2+O_3 \rightarrow OH+2O_2$ (R23), $H+HO_2 \rightarrow 2OH$ (R14), $NO+HO_2 \rightarrow NO_2+OH$ (R50), $H_2O_2+O \rightarrow OH+HO_2$ (R19), $H+NO_2 \rightarrow OH+NO$ (R51), $O(^1D)+H_2O \rightarrow 2OH$ (R7), $O(^1D)+H_2 \rightarrow H+OH$ (R8), $CH_4+O(^1D) \rightarrow CH_3+OH$ (R9),

whereas chemical sinks of this component are as follows:

$OH+O \rightarrow H+O_2$ (R17), $OH+O_3 \rightarrow O_2+HO_2$ (R22), $OH+HO_2 \rightarrow H_2O+O_2$ (R28), $OH+OH \rightarrow H_2O+O$ (R26), $OH+OH+M \rightarrow H_2O_2+M$ (R27), $H+OH+N_2 \rightarrow H_2O+N_2$ (R24), $H_2O_2+OH \rightarrow H_2O+HO_2$ (R29), $OH+CO \rightarrow H+CO_2$ (R32), $CH_4+OH \rightarrow CH_3+H_2O$ (R33), $OH+H_2 \rightarrow H_2O+H$ (R25), $N+OH \rightarrow NO+H$ (R49).

Thus, OH local equilibrium concentration is described by the following equation:

$$OH^{eq} = (k_{21} \cdot H \cdot O_3 + k_{18} \cdot O \cdot HO_2 + k_{23} \cdot HO_2 \cdot O_3 + 2 \cdot k_{14} \cdot H \cdot HO_2 + k_{50} \cdot HO_2 \cdot NO + k_{19} \cdot H_2O_2 \cdot O + k_{24} \cdot H \cdot N_2 + k_{51} \cdot NO_2 \cdot H + 2 \cdot k_7 \cdot O(^1D) \cdot H_2O + k_8 \cdot O(^1D) \cdot H_2 + k_9 \cdot O(^1D) \cdot CH_4) / (k_{17} \cdot O + k_{22} \cdot O_3 + k_{28} \cdot HO_2 + 2 \cdot (k_{26} + k_{27} \cdot M) \cdot OH + k_{29} \cdot H_2O_2 + k_{32} \cdot CO + k_{33} \cdot CH_4 + k_{25} \cdot H_2 + k_{25} \cdot N) \quad (6)$$

Figure 2 shows height-latitude cross sections for the $< OH/OH^{eq} >$ ratio for each month. In this case the equilibrium covers up to 70-80% of the presented ranges of heights and latitudes, so that the black solid lines mark the external boundaries of non-equilibrium areas. In March and September this area is almost symmetrical to the equator. In April-August it is shifted towards the northern hemisphere. In October-February this area is higher in the southern hemisphere. In all months it is below 85-86 km. In

the polar regions there are latitudinal ranges, where OH is close to equilibrium throughout the entire range of heights.

4 The main reactions, determining HO_2 and OH equilibria

Figure 3 presents height-latitude contour maps, showing the relative contribution of a certain reaction to the total source and sink of HO_2 in January, taken as an example. To increase the information content of the panels, the altitude range is cut off everywhere to 10^{-3} hPa, since there are no significant changes above. Note firstly, that reaction $H+O_2+M \rightarrow HO_2+M$ determines a major (up to 95% and more) contribution in the main equilibrium area almost everywhere, except for the polar regions above 70-75° of latitude and below 75-80 km, where the reactions $OH+O_3 \rightarrow O_2+HO_2$ and $H_2O_2+OH \rightarrow H_2O+HO_2$ become important and should be taken into account. Other reactions ($H_2O_2+O \rightarrow OH+HO_2$, $CHO+O_2 \rightarrow HO_2+CO$, $CH_3O+O_2 \rightarrow CH_2O+HO_2$) together contribute less than 2-3% to the total source of HO_2 in the main equilibrium area and may be omitted. Secondly, the reaction $HO_2+O \rightarrow OH+O_2$ determines a major (up to 95% and more) contribution to the total sink in the main equilibrium area almost everywhere, except for the same small polar areas, as in the considered case with the sources, where the reactions $HO_2+O_3 \rightarrow OH+2O_2$ and $NO+HO_2 \rightarrow NO_2+OH$ are important and should be taken into account. The reactions $OH+HO_2 \rightarrow H_2O+O_2$, $H+HO_2 \rightarrow 2OH$, $H+HO_2 \rightarrow H_2O+O$, and $H+HO_2 \rightarrow H_2+O_2$ contribute cumulatively up to 10-15% of the total sink near the boundary of the main equilibrium area. The remaining reactions ($HO_2+HO_2 \rightarrow H_2O_2+O_2$, $HO_2+HO_2+M \rightarrow H_2O_2+O_2+M$) are not important in the main equilibrium area and can be omitted. The complete figures for HO_2 sources and sinks for every month (all 12 panels) are given in Supplement (Figs. S3-S11).

Therefore, the expression for HO_2 local equilibrium concentration can be simplified as follows:

$$HO_2^{eq} = \frac{k_{20} \cdot H \cdot M \cdot O_2 + k_{22} \cdot OH \cdot O_3 + k_{29} \cdot H_2O_2 \cdot OH}{k_{18} \cdot O + k_{23} \cdot O_3 + k_{28} \cdot OH + (k_{14} + k_{15} + k_{16}) \cdot H + k_{50} \cdot NO} \quad (7)$$

Figure 4 presents height-latitude contour maps, showing the relative contribution of a certain reaction to the total source and sink of OH in January, taken as an example in Figure 3. As in the previous case, the altitude range is cut off at 10^{-3} hPa, because only the panels for the reactions $H+O_3 \rightarrow OH+O_2$ and $HO_2+O \rightarrow OH+O_2$ consist of interesting variations above. Note, that firstly these reactions are the main OH sources in the upper part of the presented distributions down to 70-75 km, where they jointly provide up to a 95% contribution to the equilibrium concentration. Also the reaction $HO_2+O_3 \rightarrow OH+2O_2$ is major source in the lower part of the presented distribution from 50 to 60-70 km. The reaction $NO+HO_2 \rightarrow NO_2+OH$ is important around non-equilibrium areas of OH and should be taken into account, whereas the reaction $H+NO_2 \rightarrow OH+NO$ is important in compact altitude-latitude areas near the

poles, the reaction $H+HO_2 \rightarrow 2OH$ gives up to 10-15% contribution in small areas near the equilibrium boundary. Other reactions ($O(^1D)+H_2O \rightarrow 2OH$, $O(^1D)+H_2 \rightarrow H+OH$, $CH_4+O(^1D) \rightarrow CH_3+OH$, $H_2O_2+O \rightarrow OH+HO_2$) together contribute less than 2-3% of the total source of OH in the main equilibrium area and can be omitted. Secondly, the reaction $OH+O \rightarrow H+O_2$ is the main OH sink in the upper part of the presented distributions down to 70-80 km, where it provides up to 95% of the equilibrium concentration. The reactions $OH+CO \rightarrow H+CO_2$ and $OH+O_3 \rightarrow O_2+HO_2$ are major in the lower part of the presented distributions from 50 to 70-80 km. The reaction $OH+HO_2 \rightarrow H_2O+O_2$ is significant enough around non-equilibrium areas of OH, whereas the reaction $H_2O_2+OH \rightarrow H_2O+HO_2$ is important in the compact altitude-latitude area near the poles. Other reactions ($OH+OH \rightarrow H_2O+O$, $OH+H_2 \rightarrow H_2O+H$, $N+OH \rightarrow NO+H$, $CH_4+OH \rightarrow CH_3+H_2O$, $H+OH+N_2 \rightarrow H_2O+N_2$, $OH+OH+M \rightarrow H_2O_2+M$) together contribute less than 2-3% to the total sink of OH in the main equilibrium area and can be omitted. The complete figures for OH sources and sinks for every month (all 12 panels) are given in Supplement (Figs. S12-S24).

Therefore, the expression for OH local equilibrium concentration can be simplified as follows:

$$OH^{eq} = \frac{k_{21}\cdot H\cdot O_3+k_{18}\cdot O\cdot HO_2+k_{23}\cdot HO_2\cdot O_3+2\cdot k_{14}\cdot H\cdot HO_2+k_{24}\cdot H\cdot N_2+k_{50}\cdot HO_2\cdot NO+k_{51}\cdot NO_2\cdot H}{k_{17}\cdot O+k_{22}\cdot O_3+k_{28}\cdot HO_2+k_{29}\cdot H_2O_2+k_{32}\cdot CO} \quad (8)$$

5 Shortened equilibrium conditions of HO_2 and OH in the upper mesosphere and lower thermosphere

The above analysis revealed, that the reactions describing the equilibrium conditions (7-8) in the lower and middle mesosphere are different from those in the upper mesosphere and lower thermosphere. This means that the task of applying these conditions can be divided into two parts depending on the selected altitude range. At the upper mesosphere and lower thermosphere altitudes, we can consider only the $HO_x - O_x$ chemistry, excluding the reactions with participation of H_2O_2, N, NO, NO_2, and CO. In addition, we can omit the reactions $HO_2+O_3 \rightarrow OH+2O_2$, $OH+O_3 \rightarrow O_2+HO_2$, and $OH+HO_2 \rightarrow H_2O+O_2$ due to their insignificance here. As a result, the shortened equilibrium conditions of HO_2 and OH for this altitude range are as follows:

$$HO_{2\,sh}^{eq} = \frac{k_{20}\cdot H\cdot M\cdot O_2}{k_{18}\cdot O+(k_{14}+k_{15}+k_{16})\cdot H}, \quad (9)$$

$$OH_{sh}^{eq} = \frac{k_{21}\cdot H\cdot O_3+k_{18}\cdot O\cdot HO_2+2\cdot k_{14}\cdot H\cdot HO_2}{k_{17}\cdot O} \quad (10)$$

Figure 5 shows height-latitude cross sections for the $< HO_2/HO_{2\,sh}^{eq} >$ ratio for each month. In each panel the upper longest black line marks the lower boundary of the main equilibrium area, where

according to condition (1) $HO_2 \approx HO_{2_{sh}}^{eq}$ with possible bias of less than 10%. As in the case of Figure 1, this area extends from the top of the analyzed altitude range. There are also very small equilibrium areas below, which can be omitted from our consideration. The height of the lower boundary of the main equilibrium area, $z_{HO_{2_{sh}}^{eq}}$, depends essentially on the season and latitude. Comparing with Figure 1 one can see, that it reproduces many features of $z_{HO_{2_{sh}}^{eq}}$ at low and middle latitudes. In particular, $z_{HO_{2_{sh}}^{eq}}$ varies in the interval between 73 and 85 km, as in the case of $z_{HO_2^{eq}}$. In the middle latitudes $z_{HO_{2_{sh}}^{eq}}$ in summer is several km higher than in winter. Near the equator $z_{HO_{2_{sh}}^{eq}}$ demonstrates the weakest annual variations and varies in the range of 81-83 km. So, one can conclude, that the exclusion of a number of reactions does not lead to significant changes in the space-time distributions of the HO_2 equilibrium.

Figure 6 plots height-latitude cross sections for the $< OH/OH_{sh}^{eq} >$ ratio for each month. As in the previous case, this is the lower boundary of the equilibrium area, where according to condition (1) $OH \approx OH_{sh}^{eq}$ with good precision. The dependence of the boundary height, $z_{OH_{sh}^{eq}}$, on the season and latitude mainly repeats the behavior of $z_{HO_{2_{sh}}^{eq}}$. In particular $z_{OH_{sh}^{eq}}$ varies in the interval between 73 and 85 km. At middle latitudes $z_{OH_{sh}^{eq}}$ in summer is several km higher than in winter. Near the equator $z_{OH_{sh}^{eq}}$ also demonstrates the weakest annual variations and varies in the range of 81-83 km. Nevertheless, in some cases the OH equilibrium boundary lies slightly higher than the HO_2 boundary. In particular it can be seen in April-August above 50ºS, which can be explained by the difference between HO_2 and OH lifetimes ($\tau_{HO_2} < \tau_{OH}$), mainly due to $k_{18} > k_{17}$. Comparing with Figure 2, one can see the exclusion of the mentioned reactions from consideration results in the absence of the OH equilibrium areas at the low and middle mesosphere altitudes, as expected.

6 The criteria for HO_2 and OH equilibrium validity in the upper mesosphere and lower thermosphere

Firstly we determine HO_2 and OH lifetimes and the local time scales of $HO_{2_{sh}}^{eq}$ and OH_{sh}^{eq}, according to Section 2.

From Eqs. (2-3) and (9), HO_2 lifetime and the local time scales of $HO_{2_{sh}}^{eq}$ are as follows:

$$\tau_{HO_2} = \frac{1}{k_{18} \cdot O + (k_{14} + k_{15} + k_{16}) \cdot H}, \quad (11)$$

$$\tau_{HO_{2_{sh}}^{eq}} = \frac{HO_{2_{sh}}^{eq}}{|dHO_{2_{sh}}^{eq}/dt|}. \quad (12)$$

Then we find the expression for $dHO_{2_{sh}}^{eq}/dt$:

306 $$\frac{dHO_{2_{sh}}^{eq}}{dt} = \frac{k_{18}\cdot k_{20}\cdot M\cdot O_2\cdot \frac{d}{dt}(\frac{H}{O})\cdot O^2}{(k_{18}\cdot O+(k_{14}+k_{15}+k_{16})\cdot H)^2} = -\frac{k_{18}\cdot k_{20}\cdot M\cdot O_2\cdot \frac{d}{dt}(\frac{O}{H})\cdot H^2}{(k_{18}\cdot O+(k_{14}+k_{15}+k_{16})\cdot H)^2}.$$ (13)

307 Kulikov et al. (2023a) analyzed the local nighttime evolution of O and H within the framework of pure
308 $HO_x - O_x$ chemistry and found the expression for $\frac{d}{dt}(\frac{O}{H})$:

309 $$\frac{d}{dt}\left(\frac{O}{H}\right) = -2\cdot k_{20}\cdot M\cdot O_2\cdot\left(1-\frac{k_{15}+k_{16}}{k_{18}}\right) - k_{21}\cdot O_3 - k_{12}\cdot M\cdot O_2\cdot\frac{O}{H}.$$ (14)

310 Thus, Eq. (13) can be rewritten in the following form:

311 $$\frac{dHO_{2_{sh}}^{eq}}{dt} = \frac{k_{18}\cdot k_{20}\cdot M\cdot O_2\cdot H^2\cdot(2\cdot k_{20}\cdot M\cdot O_2\cdot\left(1-\frac{k_{15}+k_{16}}{k_{18}}\right)+k_{21}\cdot O_3+k_{12}\cdot M\cdot O_2\cdot\frac{O}{H})}{(k_{18}\cdot O+(k_{14}+k_{15}+k_{16})\cdot H)^2}.$$ (15)

312 By combining Eqs. (9), (12), and (15) we obtain the expression for the local time scales of $HO_{2_{sh}}^{eq}$:

313 $$\tau_{HO_{2_{sh}}^{eq}} = \frac{(k_{18}\cdot O+(k_{14}+k_{15}+k_{16})\cdot H)}{k_{18}\cdot H\cdot(2\cdot k_{20}\cdot M\cdot O_2\cdot\left(1-\frac{k_{15}+k_{16}}{k_{18}}\right)+k_{21}\cdot O_3+k_{12}\cdot M\cdot O_2\cdot\frac{O}{H})}$$ (16)

314 Thus, taking into account Eqs. (4), (11) and (16), the criterion for HO_2 equilibrium validity is written in
315 the form:

316 $$Crit_{HO_2} = \frac{\tau_{HO_2}}{\tau_{\tau_{HO_{2_{sh}}^{eq}}}} = \frac{k_{18}\cdot H\cdot(2\cdot k_{20}\cdot M\cdot O_2\cdot\left(1-\frac{k_{15}+k_{16}}{k_{18}}\right)+k_{21}\cdot O_3+k_{12}\cdot M\cdot O_2\cdot\frac{O}{H})}{(k_{18}\cdot O+(k_{14}+k_{15}+k_{16})\cdot H)^2} \leq 0.1.$$ (17)

317 We calculated $Crit_{HO_2}$, using the global 3D chemical transport model, and included the zonally and
318 monthly averaged lines $< Crit_{HO_2} >= 0.1$ in Figure 5 (see magenta lines). One can see that, depending
319 on the month, each magenta line reproduces well the lower boundary of the main HO_2 equilibrium area
320 and follows almost all its features and variations. Note, that in the zeroth order approximation the
321 criterion (17) can be simplified as

322 $$Crit_{HO_2} \approx \left(2\cdot k_{20}\cdot M\cdot O_2\cdot\left(1-\frac{k_{15}+k_{16}}{k_{18}}\right)+k_{21}\cdot O_3+k_{12}\cdot M\cdot O_2\cdot\frac{O}{H}\right)\cdot\frac{H}{k_{18}\cdot O^2} \leq 0.1.$$ (18)

323 From Eqs. (2-3) and (10), OH lifetime and the local time scales of OH_{sh}^{eq} are as follows:

324 $$\tau_{OH} = \frac{1}{k_{17}\cdot O},$$ (19)

325 $$\tau_{OH_{sh}^{eq}} = \frac{OH_{sh}^{eq}}{|dOH_{sh}^{eq}/dt|}.$$ (20)

326 Before determining the expression for dOH_{sh}^{eq}/dt one should keep in mind, that the expression (10)
327 depends on the HO_2 concentration. As previously mentioned, near and above the OH equilibrium
328 boundary HO_2 is in equilibrium ($HO_2 \approx HO_{2_{sh}}^{eq}$) and we can use Eq. (9). In view of $k_{18}\cdot O \gg$
329 $(k_{14}+k_{15}+k_{16})\cdot H$,

$$HO_{2_{sh}}^{eq} \approx \frac{k_{20}\cdot H\cdot M\cdot O_2}{k_{18}\cdot O}\left(1-\frac{(k_{14}+k_{15}+k_{16})\cdot H}{k_{18}\cdot O}\right). \quad (21)$$

The substitution of Eq. (21) into Eq. (10) yields:

$$OH_{sh}^{eq} = k_{20}\cdot H\cdot M\cdot O_2\cdot\frac{\left(1+\frac{2\cdot k_{14}\cdot H}{k_{18}\cdot O}\right)\cdot\left(1-\frac{(k_{14}+k_{15}+k_{16})\cdot H}{k_{18}\cdot O}\right)}{k_{17}\cdot O}+\frac{k_{21}\cdot H\cdot O_3}{k_{17}\cdot O}\approx\frac{k_{20}\cdot H\cdot M\cdot O_2}{k_{17}\cdot O}\cdot\left(1+\frac{(k_{14}-k_{15}-k_{16})\cdot H}{k_{18}\cdot O}\right)+$$

$$\frac{k_{21}\cdot H\cdot O_3}{k_{17}\cdot O} \quad (22)$$

Thus, the expression for dOH_{sh}^{eq}/dt is:

$$\frac{dOH_{sh}^{eq}}{dt}=\frac{d}{dt}\left(\frac{H}{O}\right)\cdot\left(\frac{k_{20}\cdot M\cdot O_2}{k_{17}}\cdot\left(1+\frac{2\cdot(k_{14}-k_{15}-k_{16})\cdot H}{k_{18}\cdot O}\right)+\frac{k_{21}\cdot O_3}{k_{17}}\right)+\frac{k_{21}\cdot H\cdot}{k_{17}\cdot O}\frac{dO_3}{dt}. \quad (23)$$

Taking into account Eq. (14) and the differential equation for O_3 time evolution:

$$\frac{dO_3}{dt}=k_{12}\cdot M\cdot O_2\cdot O-k_{21}\cdot H\cdot O_3,$$

the expression (23) can be rewritten in following form:

$$\frac{dOH_{sh}^{eq}}{dt}=\frac{\left(2\cdot k_{20}\cdot M\cdot O_2\cdot\left(1-\frac{k_{15}+k_{16}}{k_{18}}\right)+k_{21}\cdot O_3+k_{12}\cdot M\cdot O_2\cdot\frac{O}{H}\right)\cdot H^2}{O^2}\cdot\left(\frac{k_{20}\cdot M\cdot O_2}{k_{17}}\cdot\left(1+\frac{2\cdot(k_{14}-k_{15}-k_{16})\cdot H}{k_{18}\cdot O}\right)+\frac{k_{21}\cdot O_3}{k_{17}}\right)+$$

$$\frac{k_{21}\cdot H\cdot(k_{12}\cdot M\cdot O_2\cdot O-k_{21}\cdot H\cdot O_3)}{k_{17}\cdot O}. \quad (24)$$

Thus, by combining Eqs. (4), (19), (20), (22), and (24) we obtain the expression for the criterion for OH equilibrium validity:

$$Crit_{OH}=\frac{\tau_{OH}}{\tau_{\tau_{OH_{sh}^{eq}}}}=$$

$$\frac{\left(\left(2\cdot k_{20}\cdot M\cdot O_2\cdot\left(1-\frac{k_{15}+k_{16}}{k_{18}}\right)+k_{21}\cdot O_3\frac{H}{O}+k_{12}\cdot M\cdot O_2\right)\cdot\left(k_{20}\cdot M\cdot O_2\cdot\left(1+\frac{2\cdot(k_{14}-k_{15}-k_{16})\cdot H}{k_{18}\cdot O}\right)+k_{21}\cdot O_3\right)+k_{21}\cdot(k_{12}\cdot M\cdot O_2\cdot O-k_{21}\cdot H\cdot O_3)\right)}{k_{17}\cdot O\cdot\left(k_{20}\cdot M\cdot O_2\cdot\left(1+\frac{(k_{14}-k_{15}-k_{16})\cdot H}{k_{18}\cdot O}\right)+k_{21}\cdot O_3\right)}\leq$$

0.1. (25)

We calculated $Crit_{OH}$, using the global 3D chemical transport model, and included the zonally and monthly averaged lines $< Crit_{OH} >= 0.1$ in Figure 6 (see magenta lines). One can see that, depending on the month, the magenta line almost everywhere reproduces the lower boundary of the OH equilibrium area and repeats mainly its features and variations. Nevertheless, there are a few (by latitude) narrow areas (in April-August near 70ºS and in October-December near 70ºN), where the criterion gives a few km lower position of the OH equilibrium boundary~~, these are discussed in the next section. Note~~. Our analysis revealed, that the main reason for that is the lack of OH+CO → H+CO_2 reaction among the sources of H in the corresponding differential equation of its chemical balance. In order to improve the criterion we revised the derivation of expression (14) for $\frac{d}{dt}\left(\frac{O}{H}\right)$ following to Kulikov et al. (2023a):

$$\frac{d}{dt}\left(\frac{O}{H}\right) = -2 \cdot k_{20} \cdot M \cdot O_2 \cdot \left(1 - \frac{k_{15}+k_{16}}{k_{18}}\right) - k_{21} \cdot O_3 - k_{12} \cdot M \cdot O_2 \cdot \frac{O}{H} - \frac{k_{32} \cdot CO}{k_{17} \cdot H} \cdot (k_{20} \cdot M \cdot O_2 \cdot (1 + \frac{(k_{14}-k_{15}-k_{16}) \cdot H}{k_{18} \cdot O}) + k_{21} \cdot O_3)). \quad (26)$$

As a result the corrected criterion for OH equilibrium validity is as follows:

$$Crit_{OH}{}^{m} = \frac{2 \cdot k_{20} \cdot M \cdot O_2 \cdot \left(1 - \frac{k_{15}+k_{16}}{k_{18}}\right) + k_{21} \cdot O_3 + k_{12} \cdot M \cdot O_2 \cdot \frac{O}{H} + \frac{k_{32} \cdot CO}{k_{17} \cdot H} \cdot (k_{20} \cdot M \cdot O_2 \cdot (1 + \frac{(k_{14}-k_{15}-k_{16}) \cdot H}{k_{18} \cdot O}) + k_{21} \cdot O_3))}{k_{17} \cdot O \cdot (k_{20} \cdot M \cdot O_2 \cdot (1 + \frac{(k_{14}-k_{15}-k_{16}) \cdot H}{k_{18} \cdot O}) + k_{21} \cdot O_3)} \cdot \frac{H}{O} \cdot$$

$$\left(k_{20} \cdot M \cdot O_2 \cdot \left(1 + \frac{2 \cdot (k_{14}-k_{15}-k_{16}) \cdot H}{k_{18} \cdot O}\right) + k_{21} \cdot O_3\right) + \frac{k_{21} \cdot (k_{12} \cdot M \cdot O_2 \cdot O - k_{21} \cdot H \cdot O_3)}{k_{17} \cdot O \cdot (k_{20} \cdot M \cdot O_2 \cdot (1 + \frac{(k_{14}-k_{15}-k_{16}) \cdot H}{k_{18} \cdot O}) + k_{21} \cdot O_3)} \leq 0.1 \quad (27)$$

We calculated this criterion, using the global 3D chemical transport model and included the zonally and monthly averaged lines $< Crit_{OH}{}^{m} >= 0.1$ on the OH equilibrium maps (see Figure 7). One can see that, the inclusion of this additional term actually eliminates the noted discrepancy between OH boundary and criterion. But the application of this criterion requires CO data.

Note also, that our numerical analysis shows that in the zeroth order approximation the criterion (25) can be simplified as:

$$Crit_{OH} \approx \left(2 \cdot k_{20} \cdot M \cdot O_2 \cdot \left(1 - \frac{k_{15}+k_{16}}{k_{18}}\right) + k_{21} \cdot O_3 + k_{12} \cdot M \cdot O_2 \cdot \frac{O}{H}\right) \cdot \frac{H}{k_{17} \cdot O^2} \leq 0.1. \quad (2628)$$

7 Discussion

We now discuss obtained results and their possible applications.

Pay attention to the fact, that the presented results were plotted, using the lower threshold at 105° for the nighttime solar zenith angle (χ) to exclude the twilight transition processes. Nevertheless, our additional analysis revealed, that OH and HO_2 equilibrium conditions are fulfilled at χ>95°.° (see Figs. S1-S2 and S25-S26 in Supplement). Evidently, during the processing of the measurement data, taking twilight χ in (95°,105°) range into account extends the latitude range of OH and HO_2 equilibria application and allows us to include a noticeable part of the data into consideration. However, in this case one should check for additional condition (Kulikov et al., 2023a):

$$e^{\int_{lt_{bn}}^{lt} \tau_{HO_2}{}^{-1} dt} \gg 1, \qquad e^{\int_{lt_{bn}}^{lt} \tau_{OH}{}^{-1} dt} \gg 1, \quad (2729)$$

where τ_{HO_2} and τ_{OH} are the HO_2 and OH lifetimes, determined by Eqs. (11) and (19), lt is local time of data, lt_{bn} is the local time at the beginning of the night. Mind, that at night O and H tend to decrease due to the shutdown of the O_x and HO_x family photochemical sources, so τ_{HO_2} and τ_{OH} increase. Thus, analyzing the measurement data one can apply more stringent conditions:

$$e^{\frac{lt-lt_{bn}}{\tau_{HO_2}}} \gg 1, \qquad e^{\frac{lt-lt_{bn}}{\tau_{OH}}} \gg 1. \quad (28\,30)$$

The main results were obtained using a 3D model, where temperature and wind distributions are updated every 24 hours. This excluded the influence of the atmospheric wave motion, in particular, associated with tides, which is one of the main dynamical drivers in the tropical mesopause. We carried out additional modeling with the distributions of the main characteristics, calculated by the Canadian Middle Atmosphere Model for the year 2009 (Scinocca et al., 2008) with a 6-hourly frequency for updating. The analysis of the time-height evolution of OH and HO_2, especially at low latitudes, showed that our criteria reproduce quite well the local variations of the OH and HO_2 equilibrium boundaries in such conditions. (see Fig. S27 in Supplement).

We evaluated the sensitivity of the presented HO_2 and OH criteria ($Crit_{HO_2}$ and $Crit_{OH}$) to the uncertainties of characteristics, involved in the expressions (17) and (25). The local heights of the OH and HO_2 equilibrium boundaries (${z_{HO_2}}^{crit}$ and ${z_{OH}}^{crit}$) according to the criteria are determined as the altitudes, at which $Crit_{HO_2} = 0.1$ and $Crit_{OH} = 0.1$ respectively. We considered the whole dataset of nighttime profiles, obtained by the numerical simulation of a one-year global evolution of mesosphere – lower thermosphere, and estimated total uncertainties to determination of ${z_{HO_2}}^{crit}$ and ${z_{OH}}^{crit}$ from each local (in time and space) dataset (profiles of O, H, O_3, M, O_2 and temperature). Following the typical analysis presented, for example in Mlynczak et al. (2013a, 2014), each uncertainty was calculated as a root sum square of the sensitivities to the individual perturbations of certain variables or parameters in the expressions (17) and (25). The following uncertainties of the variables were used: 5K in the temperature and 30% in O_3, O, and H. The uncertainties in reaction rates and their temperature dependencies were taken from Burkholder et al. (2020). As the result (see Figure 7<u>8</u>), the monthly and longitudinally mean of total uncertainties in determination of ${z_{HO_2}}^{crit}$ and ${z_{OH}}^{crit}$ were found varying in the range 0.02-1 km, depending on altitude and season. Note, that these values are comparable with the typical height resolution of satellite data. The latter allows us to consider our criteria as a robust instrument for equilibrium condition validation. The main reason of relatively low sensitivity of ${z_{HO_2}}^{crit}$ and ${z_{OH}}^{crit}$ is the strong height-dependence of $Crit_{HO_2}$ and $Crit_{OH}$ near the value of 0.1. (see Fig. S28 in Supplement).

As noted, Figs. 5-6 represent an interesting peculiarity. At the middle latitudes summer $z_{HO_{2_{sh}}^{eq}}$ and $z_{OH_{sh}^{eq}}$ are remarkably higher than winter ones. For example, in February $z_{HO_{2_{sh}}^{eq}}$ at 60ºN is ~ 84 km, whereas the one at 60ºS is ~ 74 km. Recently, Kulikov et al. (2023b) found such a feature in the evolution of nighttime ozone chemical equilibrium boundary~~,~~ (Fig. 5 there), derived from SABER/TIMED data~~, which was accompanied by~~ . The study showed that the ~~same variation of~~boundary closely follows the transition zone~~, separating deep~~ that separates strong and weak ~~photochemical~~ diurnal oscillations of O and H~~, caused by~~ (see Figs. 1-3 and 13 in Kulikov et al. (2023b)). Above the ~~diurnal variations~~zone the behavior of components is dynamically driven and seasonality is the result of ~~solar radiation. The authors analyzed this effect near and below~~ change in global-scale circulation, vertical advection being the primary factor according to Wang et al. (2023). In the transition zone~~.~~ and below O and H concentrations change by orders of magnitude during the night driven by photochemical processes. Kulikov et al. (2023b) studied the photochemistry at these altitudes and its seasonal dependence. It was shown ~~firstly,~~analytically that nighttime O decreases with the characteristic time scale $\tau_O = O/|dO/dt|$ proportional to the O/H ~~ratio~~value at the beginning of the night~~. Secondly,~~ (see Eq. (13) there). At the same time, according to the distributions derived from SABER measurements O/H during ~~the~~ summer ~~the~~ daytime ~~O/H~~ (and thus also at the beginning of the night) at the middle latitudes is remarkably less than the one ~~in~~during winter~~.~~ daytime (see Fig. 14 there). Consequently, summer values of nighttime τ_O below ~ 84 km are significantly shorter than winter ones, so summer O during the night decreases much faster than in winter. In our case lifetimes of HO_2 and OH are proportional mainly to $\frac{1}{O}$ (see Eqs. (11) and (19)), so, following the approach described in Section 2, the summer rise of ~~$z_{HO_{2_{sh}}^{eq}}$~~$z_{HO_{2_{sh}}^{eq}}$ and $z_{OH_{sh}^{eq}}$ at the middle latitudes can be explained by the season difference in O diurnal photochemical evolution at these ~~latitudes~~altitudes.

~~As noted, there are a few narrow areas near 70ºS/N (Figure 6), where the criterion (25) does not correspond well to the OH equilibrium boundary. Our analysis revealed, that the main reason is neglecting the reaction OH+CO → H+CO_2 as the source of H in the corresponding differential equation of its chemical balance. In order to improve the criterion we revised the derivation of expression (14) for $\frac{d}{dt}(\frac{O}{H})$ following to Kulikov et al. (2023a):~~

~~$$\frac{d}{dt}\left(\frac{O}{H}\right) = -2 \cdot k_{20} \cdot M \cdot O_2 \cdot \left(1 - \frac{k_{15}+k_{16}}{k_{18}}\right) - k_{21} \cdot O_3 - k_{12} \cdot M \cdot O_2 \cdot \frac{O}{H} - \frac{k_{32} \cdot CO}{k_{17} \cdot H} \cdot (k_{20} \cdot M \cdot O_2 \cdot (1 + \frac{(k_{14} - k_{15} - k_{16}) H}{k_{18} O}) + k_{21} \cdot O_3)). \quad (29)$$~~

~~As a result the corrected criterion for OH equilibrium validity is as follows:~~

444 $$Crit_{OH}^{m} = \frac{2 \cdot k_{20} \cdot M \cdot O_2 \cdot \left(1 - \frac{k_{15}+k_{16}}{k_{18}}\right) + k_{21} \cdot O_3 + k_{12} \cdot M \cdot O_2 \cdot \frac{O}{H} + \frac{k_{32} \cdot CO}{k_{17} \cdot H} \cdot (k_{20} \cdot M \cdot O_2 \cdot (1 + \frac{(k_{14}-k_{15}-k_{16}) \cdot H}{k_{18} \cdot O}) + k_{21} \cdot O_3))}{k_{12} \cdot O \cdot (k_{20} \cdot M \cdot O_2 \cdot (1 + \frac{(k_{14}-k_{15}-k_{16}) \cdot H}{k_{18} \cdot O}) + k_{21} \cdot O_3)} \cdot \frac{H}{O}$$

445 $$\left(k_{20} \cdot M \cdot O_2 \cdot \left(1 + \frac{2 \cdot (k_{14}-k_{15}-k_{16}) \cdot H}{k_{18} \cdot O}\right) + k_{21} \cdot O_3\right) + \frac{k_{21} \cdot (k_{12} \cdot M \cdot O_2 \cdot O - k_{21} \cdot H \cdot O_3)}{k_{12} \cdot O \cdot (k_{20} \cdot M \cdot O_2 \cdot (1 + \frac{(k_{14}-k_{15}-k_{16}) \cdot H}{k_{18} \cdot O}) + k_{21} \cdot O_3)} \leq 0.1 \quad (30)$$

446 We calculated this criterion, using the global 3D chemical transport model and included the zonally and
447 monthly averaged lines $< Crit_{OH}^{m} >= 0.1$ on the OH equilibrium maps (see Figure 8). One can see that,
448 the inclusion of this additional term actually eliminates the noted discrepancy between OH boundary and
449 criterion. But the application of this criterion requires CO data.

450 As noted in the Introduction, the conditions of nighttime OH and HO_2 equilibria together with one
451 for O_3 equilibrium and their analytical criteria constitute a useful tool for retrieval of these components or
452 other characteristics (for example, O and H) from measured data. At the altitudes of upper mesosphere –
453 lower thermosphere these conditions can be applied, for example, to MLS/Aura database (measured
454 characteristics: OH, HO_2, O_3, and CO), SMILES (HO_2 and O_3), SCIAMACHY ($O(^1S)$ green-line, O_2 A-
455 band, and OH Meinel band emissions), SABER/TIMED (O_3, OH Meinel band emissions at 2.0 μm (9→7
456 and 8→6 bands) and at 1.6 μm (5→3 and 4→2 bands)) and other, including improvement of existing
457 retrieval approaches. In particular, Panka et al. (2021) proposed the method of simultaneous derivation of
458 O and OH at the levels v=0-9 from SABER data (volume emission rates at 2.0 and 1.6 μm, $VER_{2\mu m}$ and
459 $VER_{1.6\mu m}$) at 80-100 km, taking into account the equilibrium condition for all states of OH. Such
460 approach is valid for excited states due to their very short lifetimes determined by radiative transitions
461 and quenching with O_2, N_2, and O. In the case of the OH ground state its lifetime is determined by the
462 reaction OH+O → H+O_2 only. It means, that Panka et al. (2021) used an equilibrium condition for total
463 OH, which, as one can see from Figure 6, may be significantly disrupted above 80 km. On the other hand,
464 there are latitude ranges and months, when the OH equilibrium boundary drops remarkably below 80 km.
465 Moreover, the Panka et al. method requires external data about HO_2, since the reaction HO_2+O → OH+O_2
466 becomes the important source for OH below 87 km (Panka et al., 2021; see also Figure 4 in our paper).

467 The results of our paper allow modifying the Panka et al. method to extend its capabilities. The
468 simplest development of this method seems to be the following. First of all, note that the HO_2 equilibrium
469 condition (9) depends on H and O only and can be used within the self-consistent retrieval procedure,
470 considering the following system of equations:

471 $$OH(v = 1-9) = \frac{k_{12} \cdot H \cdot O_3 \cdot M \cdot f(v) + \sum_{v'>v} (a_1(v',v) + a_2(v',v) \cdot O_2 + a_3(v',v) \cdot N_2 + (a_4(v',v) + a_5(v',v)) \cdot O) \cdot OH(v')}{a_6(v)) \cdot O + \sum_{v>v'} (a_1(v,v') + a_2(v,v') \cdot O_2 + a_3(v,v') \cdot N_2 + (a_4(v,v') + a_5(v,v')) \cdot O)},$$

472 $$OH(0) = \frac{\sum_{v'>0} (a_1(v',0) + a_2(v',0) \cdot O_2 + a_3(v',0) \cdot N_2 + (a_4(v',0) + a_5(v',0)) \cdot O) \cdot OH(v') + k_{18} \cdot O \cdot HO_2 + 2 \cdot k_{14} \cdot H \cdot HO_2}{k_{17} \cdot O},$$

473 $$HO_2 = \frac{k_{20} \cdot H \cdot M \cdot O_2}{k_{18} \cdot O + (k_{14} + k_{15} + k_{16}) \cdot H},$$

474 $$VER_{2\mu m} = a_1(9,7) \cdot OH(9) + a_1(8,9) \cdot OH(8),$$

$$VER_{1.6\mu m} = a_1(5,3) \cdot OH(5) + a_1(4,2) \cdot OH(4),$$

where a_{1-6} are the constant rates of the processes OH(v) → OH(v'<v) + hv, OH(v) +O_2 → OH(v<v') + O_2, OH(v) +N_2 → OH(v<v') + N_2, OH(v) +O(^{3}P) → OH(v'≤v-5) + O(^{1}D), OH(v) +O(^{3}P) → OH(v'<v) + O(^{3}P), and OH(v) +O(^{3}P) → H + O_2 respectively. Take into consideration, that this system includes 13 equations with 13 unknown variables. Therefore, the solution to the system for a single set of the SABER measurements (simultaneously measured profiles of O_3, T, pressure, $VER_{2\mu m}$, and $VER_{1.6\mu m}$) gives one simultaneously retrieved profiles of O, H, OH(v=0-9), and HO_2. By applying the criteria (17) and (25) to obtained O and H profiles, we verify the fulfillment of OH and HO_2 equilibrium conditions and determine the height, below which the resulting profiles should be cut. More advanced retrieval procedure would be statistical, based on Bayesian theorem, taking into account the uncertainties in measurement data and rate constants. Similarly, for example, to Kulikov et al. (2018a), it should include a derivation of posterior conditional probability density function of retrieved characteristics and numerical analysis of this function. Detailed development of this retrieval method is outside of this paper and should be carried out in a separate work.

8 Conclusions

The presented analysis shows, that there are extended areas in mesosphere and lower thermosphere, where nighttime HO_2 and OH are close to their local equilibrium concentrations, determined mainly by the reactions between HO_x – O_x components among themselves and with H_2O_2, N, NO, NO_2, and CO. In upper mesosphere – lower thermosphere the shortened expressions for their local equilibrium concentrations are valid, including the HO_x – O_x chemistry only. These conditions describe the HO_2 and OH equilibrium from the top to some lower boundaries, the altitude position of which vary in the interval between 73 and 85 km and depends essentially on the season and latitude. We proposed analytical criteria, which almost everywhere reproduces quite well the main features of these boundaries. Due to weak sensitivity to uncertainties of reaction rates and variables, these criteria can be considered a robust instrument for HO_2 and OH equilibrium validation. The obtained results allow extending the abilities of the Panka et al. (2021) method to retrieve unmeasured components from SABER data. The simultaneous application of OH and HO_2 equilibrium conditions to the SABER data together with the OH and HO_2 criteria to control this equilibrium validity allows us to retrieve all unknown HO_x – O_x components (O, H, OH, and HO_2) and to extend the altitude range of retrieval downward below 80 km and without external information.

Data availability. CMAM data are obtained from the website (https://climate-modelling.canada.ca/climatemodeldata/cmam/cmam30/, last access: ~~18 May~~31 July 2024).

Code availability. Code is available upon request.

Author contributions. Conceptualization: MK, MB, AC, SD, AF. Methodology: MK, AF. Investigation: MK, MB, AC, SD. Software: MB, AC. Visualization: MB, AC. Funding Acquisition: MK. Writing – original draft preparation: MK, MB. Writing – review & editing: AC, SD. Supervising: AF.

Competing interests. The authors declare no conflict of interest.

Acknowledgements. The paper is in the memory of Prof. G.M. Fraiman. The authors are grateful to reviewers for providing valuable recommendations to improve the paper.

Financial support. The main results presented in Sects. 3-6 were obtained with the support of the Russian Science Foundation under grant No. 22-12-00064 (https://rscf.ru/project/22-12-00064/, last access: ~~18 May~~31 July 2024). The analysis in Discussion was carried out at the expense of state assignment No. 0729-2020-0037.

Supplement link:

References

Avallone, L. M. and Toohey, D. W.: Tests of halogen photochemistry using in situ measurements of ClO and BrO in the lower polar stratosphere, J. Geophys. Res., 106, 10411–1042, https://doi.org/10.1029/2000JD900831, 2001.

Belikovich, M. V., Kulikov, M. Yu, Grygalashvyly, M., Sonnemann, G. R., Ermakova, T. S., Nechaev, A. A., and Feigin, A .M.: Ozone chemical equilibrium in the extended mesopause under the nighttime conditions, Adv. Space Res., 61, 426–432, https://doi.org/10.1016/j.asr.2017.10.010, 2018.

Berger, U., and U. von Zahn (1999), Two level structure of the mesopause: A model study, *J. Geophys. Res.*, 104, 22,083–22,093.

Burkholder, J. B., Sander, S. P., Abbatt, J., Barker, J. R., Cappa, C., Crounse, J. D., Dibble, T. S., Huie, R. E., Kolb, C. E., Kurylo, M. J., Orkin, V. L., Percival, C. J., Wilmouth, D. M., and Wine, P. H.: Chemical Kinetics and Photochemical Data for Use in Atmospheric Studies, Evaluation No. 19, JPL Publication 19-5, Jet Propulsion Laboratory, Pasadena, http://jpldataeval.jpl.nasa.gov, 2020.

Cantrell, C. A., Mauldin, L., Zondlo, M., Eisele, F., Kosciuch, E., Shetter, R., Lefer, B., Hall, S., Campos, T., Ridley, B., Walega, J., Fried, A., Wert, B., Flocke, F., Weinheimer, A., Hannigan, J., Coffey, M., Atlas, E., Stephens, S., Heikes, B., Snow, J., Blake, D., Blake, N., Katzenstein, A., Lopez, J., Browell, E. V., Dibb, J., Scheuer, E., Seid, G., and Talbot, R.: Steady state free radical budgets and ozone photochemistry during TOPSE, J. Geophys. Res., 108, TOP9-1–TOP9-22, https://doi.org/10.1029/2002JD002198, 2003.

Evans, W. F. J., and Llewellyn, E. J.: Atomic hydrogen concentrations in the mesosphere and the hydroxyl emissions, J. Geophys. Res., 78, 323–326, https://doi.org/1010.1029/JA078i001p00323, 1973.

Evans, W. F. J., McDade, I. C., Yuen, J., and Llewellyn, E. J.: A rocket measurement of the O_2 infrared atmospheric (0-0) band emission in the dayglow and a determination of the mesospheric ozone and atomic oxygen densities, Can. J. Phys., 66, 941–946, https://doi.org/10.1139/p88-151. 1988.

Fytterer, T., von Savigny, C., Mlynczak, M., and Sinnhuber, M.: Model results of OH airglow considering four different wavelength regions to derive night-time atomic oxygen and atomic hydrogen in the mesopause region, Atmos. Chem. Phys., 19, 1835–1851, https://doi.org/10.5194/acp-19-1835-2019, 2019.

Good, R. E.: Determination of atomic oxygen density from rocket borne measurements of hydroxyl airglow, Planet. Space Sci., 24, 389–395, https://doi.org/10.1016/0032-0633(76)90052-0, 1976.

Grygalashvyly, M., Sonnemann, G. R., and Hartogh, P.: Long-term behavior of the concentration of the minor constituents in the mesosphere - a model study, Atmos. Chem. Phys., 9, 2779–2792, https://doi.org/10.5194/acp-9-2779-2009, 2009.

Grygalashvyly, M., Sonnemann, G. R., Lübken, F.-J., Hartogh, P., and Berger, U.: Hydroxyl layer: Mean state and trends at midlatitudes, J. Geophys. Res. Atmos., 119, 12,391–12,419, https://doi.org/10.1002/2014JD022094, 2014.

Grygalashvyly, M.: Several notes on the OH* layer, Ann. Geophys., 33, 923-930, https://doi.org/10.5194/angeo-33-923-2015, 2015.

Hartogh, P., Jarchow, C., Sonnemann, G. R., and Grygalashvyly, M.: On the spatiotemporal behavior of ozone within the upper mesosphere/mesopause region under nearly polar night conditions, J. Geophys. Res., 109, D18303, https://doi.org/10.1029/2004JD004576, 2004.

Hartogh, P., Jarchow, Ch., Sonnemann, G. R., and Grygalashvyly, M.: Ozone distribution in the middle latitude mesosphere as derived from microwave measurements at Lindau (51.66°N, 10.13°E), J. Geophys. Res., 116, D04305, https://doi.org/10.1029/2010JD014393, 2011.

Körner, U., and Sonnemann, G. R.: Global 3D-modeling of water vapor concentration of the mesosphere/mesopause region and implications with respect to the NLC region, J. Geophys. Res., 106, 9639– 9651, https://doi.org/10.1029/2000JD900744, 2001.

Kowalewski, S., v. Savigny, C., Palm, M., McDade, I. C., and Notholt, J.: On the impact of the temporal variability of the collisional quenching process on the mesospheric OH emission layer: a study based on SD-WACCM4 and SABER, Atmos. Chem. Phys., 14, 10193-10210, https://doi.org/10.5194/acp-14-10193-2014, 2014.

Kremp, C., Berger, U., Hoffmann, P., Keuer, D., and Sonnemann, G. R.: Seasonal variation of middle latitude wind fields of the mesopause region—A comparison between observation and model calculation, Geophys. Res. Lett., 26, 1279–1282, https://doi.org/10.1029/1999GL900218, 1999.

Kulikov, M. Y., Feigin, A. M., and Sonnemann, G. R.: Retrieval of the vertical distribution of chemical components in the mesosphere from simultaneous measurements of ozone and hydroxyl distributions, Radiophys. Quantum Electron., 49, 683–691, https://doi.org/10.1007/s11141-006-0103-4, 2006.

Kulikov, M. Yu., Feigin, A. M., and Sonnemann, G. R.: Retrieval of water vapor profile in the mesosphere from satellite ozone and hydroxyl measurements by the basic dynamic model of mesospheric photochemical system, Atmos. Chem. Phys., 9, 8199–8210, https://doi.org/10.5194/acp-9-8199-2009, 2009.

Kulikov, M. Y., Belikovich, M. V., Grygalashvyly, M., Sonnemann, G. R., Ermakova, T. S., Nechaev, A. A., and Feigin, A. M.: Daytime ozone loss term in the mesopause region, Ann. Geophys., 35, 677-682 https://doi.org/10.5194/angeo-35-677-2017, 2017.

Kulikov, M. Y., Nechaev, A. A., Belikovich, M. V., Ermakova, T. S., and Feigin, A. M.: Technical note: Evaluation of the simultaneous measurements of mesospheric OH, HO_2, and O_3 under a photochemical equilibrium assumption – a statistical approach, Atm. Chem. Phys., 18, 7453-747, https://doi.org/10.5194/acp-18-7453-2018, 2018a.

Kulikov, M. Y., Belikovich, M. V., Grygalashvyly, M., Sonnemann, G. R., Ermakova, T. S., Nechaev, A. A., and Feigin, A. M.: Nighttime ozone chemical equilibrium in the mesopause region. J. Geophys. Res.,123, 3228–3242, https://doi.org/10.1002/2017JD026717, 2018b.

Kulikov, M. Yu., Nechaev, A. A., Belikovich, M. V., Vorobeva, E. V., Grygalashvyly, M., Sonnemann, G. R., and Feigin, A. M.: Border of nighttime ozone chemical equilibrium in the mesopause region from SABER data: implications for derivation of atomic oxygen and atomic hydrogen, Geophys. Res. Lett., 46, 997– 1004, https://doi.org/10.1029/2018GL080364, 2019.

Kulikov, M. Y., Belikovich, M. V., Feigin, A. M.: The 2-day photochemical oscillations in the mesopause region: the first experimental evidence? Geophys. Res. Lett., 48, e2021GL092795, https://doi.org/10.1029/2021GL092795, 2021.

Kulikov M.Yu., Belikovich, M.V., Grygalashvyly, M., Sonnemann, G. R., and Feigin, A.M.: Retrieving daytime distributions of O, H, OH, HO_2, and chemical heating rate in the mesopause region from satellite observations of ozone and OH* volume emission: The evaluation of the importance of the reaction $H+O_3 \rightarrow O_2+OH$ in the ozone balance, Adv. Space Res., 69(9), 3362-3373, https://doi.org/10.1016/j.asr.2022.02.011, 2022a.

Kulikov, M. Y., Belikovich, M. V., Grygalashvyly, M., Sonnemann, G. R., and Feigin, A.M.: The revised method for retrieving daytime distributions of atomic oxygen and odd-hydrogens in the mesopause region from satellite observations, Earth, Planets and Space, 74, 44, https://doi.org/10.1186/s40623-022-01603-8, 2022b.

Kulikov, M. Yu., Belikovich, M. V., Chubarov, A. G., Dementeyva, S. O., Feigin, A. M.: Boundary of nighttime ozone chemical equilibrium in the mesopause region: improved criterion of determining the boundary from satellite data, Adv. Space Res., 71 (6), 2770-2780, https://doi.org/10.1016/j.asr.2022.11.005, 2023a.

Kulikov, M. Yu., Belikovich, M. V., Chubarov, A. G., Dementyeva, S. O., and Feigin, A. M.: Boundary of nighttime ozone chemical equilibrium in the mesopause region: long-term evolution determined using 20-year satellite observations, Atmos. Chem. Phys., 23, 14593–14608, https://doi.org/10.5194/acp-23-14593-2023, 2023b.

Llewellyn, E. J., McDade, I. C. Moorhouse, P. and Lockerbie M. D.: Possible reference models for atomic oxygen in the terrestrial atmosphere, Adv. Space Res., 13, 135–144, https://doi.org/10.1016/0273-1177(93)90013-2, 1993.

Llewellyn, E. J., and McDade, I. C.: A reference model for atomic oxygen in the terrestrial atmosphere, Adv. Space Res., 18, 209–226, https://doi.org/10.1016/0273-1177(96)00059-2, 1996.

Manney, G. L., Kruger, K., Sabutis, J. L., Sena, S. A., and Pawson, S.: The remarkable 2003–2004 winter and other recent warm winters in the Arctic stratosphere since the late 1990s. J. Geophys. Res., 110, D04107, https://doi.org/10.1029/2004JD005367, 2005.

Marchand, M., Bekki, S., Lefevre, F., and Hauchecorne, A.: Temperature retrieval from stratospheric O3 and NO3 GOMOS data, Geophys. Res. Lett., 34, L24809, https://doi.org/10.1029/2007GL030280, 2007.

Marsh, D. R., Smith, A. K., Mlynczak, M. G., and Russell III, J. M.: SABER observations of the OH Meinel airglow variability near the mesopause, J. Geophys. Res., 111, A10S05, https://doi.org/10.1029/2005JA011451, 2006.

McDade, I. C., Llewellyn, E. J., and Harris, F. R.: Atomic oxygen concentrations in the lower auroral thermosphere, Adv. Space Res., 5, 229–232, https://doi.org/10.1029/GL011I003P00247, 1985.

McDade, I. C., and Llewellyn, E. J.: Mesospheric oxygen atom densities inferred from night-time OH Meinel band emission rates, Planet. Space Sci., 36, 897–905, https://doi.org/10.1016/0032-0633(88)90097-9, 1988.

Mlynczak, M. G., Marshall, B. T., Martin-Torres, F. J., Russell III, J. M., Thompson, R. E., Remsberg, E. E., and Gordley, L. L.: Sounding of the Atmosphere using Broadband Emission Radiometry observations of daytime mesospheric $O_2(^1D)$ 1.27 μm emission and derivation of ozone, atomic oxygen, and solar and chemical energy deposition rates, J. Geophys. Res., 112, D15306, https://doi.org/10.1029/2006JD008355, 2007.

Mlynczak, M. G., Hunt, L. A., Mast, J. C., Marshall, B. T., Russell III, J. M., Smith, A. K., Siskind, D. E., Yee, J.-H., Mertens, C. J., Martin-Torres, F. J., Thompson, R. E., Drob, D. P., and Gordley, L. L.: Atomic oxygen in the mesosphere and lower thermosphere derived from SABER: Algorithm theoretical basis and measurement uncertainty, J. Geophys. Res., 118, 5724–5735, https://doi.org/10.1002/jgrd.50401, 2013a.

Mlynczak, M. G., Hunt, L. H., Mertens, C. J., Marshall, B. T., Russell III, J. M., López-Puertas, M., Smith, A. K., Siskind, D. E., Mast, J. C., Thompson, R. E., and Gordley, L. L.: Radiative and energetic constraints on the global annual mean atomic oxygen concentration in the mesopause region, J. Geophys. Res. Atmos., 118, 5796–5802, https://doi.org/10.1002/jgrd.50400, 2013b.

Mlynczak, M. G., Hunt, L. A. Marshall, B. T. Mertens, C. J. Marsh, D. R. Smith, A. K. Russell, J. M. Siskind D. E., and Gordley L. L.: Atomic hydrogen in the mesopause region derived from SABER: Algorithm theoretical basis, measurement uncertainty, and results, J. Geophys. Res., 119, 3516–3526, https://doi.org/10.1002/2013JD021263, 2014.

Mlynczak, M. G., Hunt, L. A., Russell, J. M. III, and Marshall, B. T.: Updated SABER night atomic oxygen and implications for SABER ozone and atomic hydrogen, Geophys. Res. Lett., 45, 5735–5741, https://doi.org/10.1029/2018GL077377, 2018.

Morton, K. W., and Mayers, D. F.; Numerical Solution of Partial Differential Equations, Cambridge University Press, 1994.

Nikoukar, R., Swenson, G. R., Liu, A. Z., and Kamalabadi, F.: On the variability of mesospheric OH emission profiles, J. Geophys. Res., 112, D19109, https://doi.org/10.1029/2007JD008601, 2007.

Panka, P. A., Kutepov, A. A., Zhu, Y., Kaufmann, M., Kalogerakis, K. S., Rezac, L., et al.: Simultaneous retrievals of nighttime $O(^3P)$ and total OH densities from satellite observations of Meinel band emissions. Geoph. Res.Lett., 48, e2020GL091053, https://doi.org/10.1029/2020GL091053, 2021.

Pendleton, W. R., Baker, K. D., Howlett, L. C.: Rocket-based investigations of $O(^3P)$, O_2 ($a^1\Delta_g$) and OH* (v=1,2) during the solar eclipse of 26 February 1979, J. Atm. Terr. Phys., 45(7), 479-491, 1983.

Siskind, D. E., Marsh, D. R., Mlynczak, M. G., Martin-Torres, F. J., and Russell III, J. M.: Decreases in atomic hydrogen over the summer pole: Evidence for dehydration from polar mesospheric clouds? Geophys. Res. Lett., 35, L13809, https://doi.org/10.1029/2008GL033742, 2008.

Russell, J. P., and Lowe, R. P.: Atomic oxygen profiles (80-94 km) derived from Wind Imaging Interferometer/Upper Atmospheric Research Satellite measurements of the hydroxyl airglow: 1. Validation of technique, J. Geophys. Res., 108(D21), 4662, https://doi.org/10.1029/2003JD003454, 2003.

677 Russell, J. P., Ward, W. E., Lowe, R. P., Roble, R. G., Shepherd, G. G., and Solheim, B.: Atomic oxygen
678 profiles (80 to 115 km) derived from Wind Imaging Interferometer/Upper Atmospheric Research Satellite
679 measurements of the hydroxyl and green line airglow: Local time–latitude dependence, J. Geophys. Res.,
680 110(D15), D15305, https://doi.org/10.1029/2004JD005570, 2005.
681 Siskind, D. E., Mlynczak, M. G., Marshall, T., Friedrich, M., Gumbel, J.: Implications of odd oxygen
682 observations by the TIMED/SABER instrument for lower D region ionospheric modeling, J. Atmos. Sol.
683 Terr. Phys., 124, 63–70, https://doi.org/10.1016/j.jastp.2015.01.014, 2015.
684 Smith, A. K., Lopez-Puertas, M., Garcıa-Comas, M. and Tukiainen, S.: SABER observations of
685 mesospheric ozone during NH late winter 2002–2009, Geophys. Res. Lett., 36, L23804,
686 https://doi.org/10.1029/2009GL040942, 2009.
687 Smith, A. K., Marsh, D. R. Mlynczak, M. G. and Mast, J. C.: Temporal variations of atomic oxygen in the
688 upper mesosphere from SABER, J. Geophys. Res., 115, D18309, https://doi.org/10.1029/2009JD013434,
689 2010.
690 Scinocca, J. F., McFarlane, N. A., Lazare, M., Li, J., and Plummer, D.: The CCCma third generation
691 AGCM and its extension into the middle atmosphere, Atmos. Chem. Phys., 8, 7055–7074,
692 https://doi.org/10.5194/acp-8-7055-2008, 2008.
693 Sonnemann, G., Kremp, C. Ebel, A. and Berger U.: A three-dimensional dynamic model of minor
694 constituents of the mesosphere, Atmos. Environ., 32, 3157–3172, https://doi.org/10.1016/S1352-
695 2310(98)00113-7, 1998.
696 Sonnemann, G. R., Grygalashvyly, M., Hartogh, P., and Jarchow, C.: Behavior of mesospheric ozone
697 under nearly polar night conditions, Adv. Space Res., 38, 2402–2407,
698 https://doi.org/10.1016/j.asr.2006.09.011, 2006.
699 Sonnemann, G. R., Hartogh, P., Grygalashvyly, M., Li, S., and Berger, U.: The quasi 5-day signal in the
700 mesospheric water vapor concentration at high latitudes in 2003-a comparison between observations at
701 ALOMAR and calculations, J. Geophys. Res., 113, D04101, https://doi.org/10.1029/2007JD008875,
702 2008.
703 Sonnemann, G. R., Hartogh, P., Berger, U., and Grygalashvyly, M.: Hydroxyl layer: trend of number
704 density and intra-annual variability, Ann. Geophys., 33, 749–767, https://doi.org/10.5194/angeo-33-749-
705 2015, 2015.
706 Stedman, D. H., Chameides, W., and Jackson, J. O.: Comparison of experimental and computed values
707 for J(NO2), Geophys. Res. Lett., 2, 22–25, https://doi.org/10.1029/GL002i001p00022, 1975.
708 Swenson, G. R., and Gardner C. S.: Analytical models for the responses of the mesospheric OH* and Na
709 layers to atmospheric gravity waves, J. Geophys. Res., 103(D6), 6271–6294,
710 https://doi.org/10.1029/97JD02985, 1998.

Thomas, R. J.: Atomic hydrogen and atomic oxygen density in the mesosphere region: Global and seasonal variations deduced from Solar Mesosphere Explorer near-infrared emissions, J. Geophys. Res., 95, 16,457–16,476, https://doi. org/ 10. 1029/ JD095 iD10p 16457, 1990.

Walcek, C. J.: Minor flux adjustment near mixing ratio extremes for simplified yet highly accurate monotonic calculation of tracer advection, J. Geophys. Res., 105, 9335-9348, https://doi.org/10.1029/1999JD901142, 2000.

Wang, J. C., Yue, J., Wang, W., Qian, L., Jones, M., Jr., and Wang, N.: The lower thermospheric winter-to-summer meridional circulation: 2. Impact on atomic oxygen J. Geophys. Res. Space Phys., 128, e2023JA031684, https://doi.org/10.1029/2023JA031684, 2023.

Xu, J., Smith, A. K., Jiang, G., Gao, H., Wei, Y., Mlynczak, M. G., and Russell III, J. M.: Strong longitudinal variations in the OH nightglow, Geophys. Res. Lett., 37, L21801, https://doi.org/10.1029/2010GL043972, 2010.

Xu, J., Gao, H. Smith, A. K. and Zhu Y.: Using TIMED/SABER nightglow observations to investigate hydroxyl emission mechanisms in the mesopause region, J. Geophys. Res., 117, D02301, https://doi.org/10.1029/2011JD016342, 2012.

Table 1. List of reactions included in 3-d chemical transport model with the corresponding reaction rates taken from Burkholder et al. (2020).

1	$O(^1D)+O_2 \rightarrow O+O_2$	24	$H+OH+N_2 \rightarrow H_2O+N_2$	47	$NO+O_3 \rightarrow NO_2+O_2$
2	$O(^1D)+N_2 \rightarrow O+N_2$	25	$OH+H_2 \rightarrow H_2O+H$	48	$NO_2+O_3 \rightarrow NO_3+O_2$
3	$O(^1D)+O_3 \rightarrow O_2+2O$	26	$OH+OH \rightarrow H_2O+O$	49	$N+OH \rightarrow NO+H$
4	$O(^1D)+O_3 \rightarrow 2O_2$	27	$OH+OH+M \rightarrow H_2O_2+M$	50	$NO+HO_2 \rightarrow NO_2+OH$
5	$O(^1D)+N_2O \rightarrow 2NO$	28	$OH+HO_2 \rightarrow H_2O+O_2$	51	$H+NO_2 \rightarrow OH+NO$
6	$O(^1D)+N_2O \rightarrow N_2+O_2$	29	$H_2O_2+OH \rightarrow H_2O+HO_2$	52	$NO_3+NO \rightarrow 2NO_2$
7	$O(^1D)+H_2O \rightarrow 2OH$	30	$HO_2+HO_2 \rightarrow H_2O_2+O_2$	53	$N+NO \rightarrow N_2+O$
8	$O(^1D)+H_2 \rightarrow H+OH$	31	$HO_2+HO_2+M \rightarrow H_2O_2+O_2+M$	54	$N+NO_2 \rightarrow N_2O+O$
9	$O(^1D)+CH_4 \rightarrow CH_3+OH$	32	$OH+CO \rightarrow H+CO_2$	55	$O_2+h\nu \rightarrow 2O$
10	$O(^1D)+CH_4 \rightarrow H_2+ CH_2O$	33	$CH_4+OH \rightarrow CH_3+H_2O$	56	$O_2+h\nu \rightarrow O+O(^1D)$
11	$O+O+M \rightarrow O_2+M$	34	$CH_3+O_2 \rightarrow CH_3O_2$	57	$O_3+h\nu \rightarrow O_2+O$
12	$O+O_2+M \rightarrow O_3+M$	35	$CH_3+O \rightarrow CH_2O+H$	58	$O_3+h\nu \rightarrow O_2+O(^1D)$
13	$O+O_3 \rightarrow O_2 +O_2$	36	$CH_3O_2+NO \rightarrow CH_3O+NO_2$	59	$N_2+h\nu \rightarrow 2N$
14	$H+HO_2 \rightarrow 2OH$	37	$CH_3O+O_2 \rightarrow CH_2O+HO_2$	60	$NO+h\nu \rightarrow N+O$
15	$H+HO_2 \rightarrow H_2O+O$	38	$CH_2O \rightarrow H_2+CO$	61	$NO_2+h\nu \rightarrow NO+O$
16	$H+HO_2 \rightarrow H_2+O_2$	39	$CH_2O \rightarrow H+CHO$	62	$N_2O+h\nu \rightarrow N_2+O(^1D)$
17	$OH+O \rightarrow H+O_2$	40	$CHO+O_2 \rightarrow HO_2+CO$	63	$N_2O+h\nu \rightarrow N+NO$
18	$HO_2+O \rightarrow OH+O_2$	41	$O_3+N \rightarrow NO+O_2$	64	$NO_3+h\nu \rightarrow NO_2+O$
19	$H_2O_2+O \rightarrow OH+HO_2$	42	$NO_3+O \rightarrow NO_2+O_2$	65	$H_2O+h\nu \rightarrow H+OH$
20	$H+O_2+M \rightarrow HO_2+M$	43	$O+NO+M \rightarrow NO_2+M$	66	$H_2O_2+h\nu \rightarrow 2OH$
21	$H+O_3 \rightarrow OH+O_2$	44	$NO_2+O \rightarrow NO+O_2$	67	$CH_4+h\nu \rightarrow CH_2+H_2$
22	$OH+O_3 \rightarrow O_2+HO_2$	45	$NO_2+O+M \rightarrow NO_3+M$	68	$CH_4+h\nu \rightarrow CH+H_2+H$
23	$HO_2+O_3 \rightarrow OH+2O_2$	46	$N+O_2 \rightarrow NO+O$	69	$CO_2+h\nu \rightarrow CO+O$

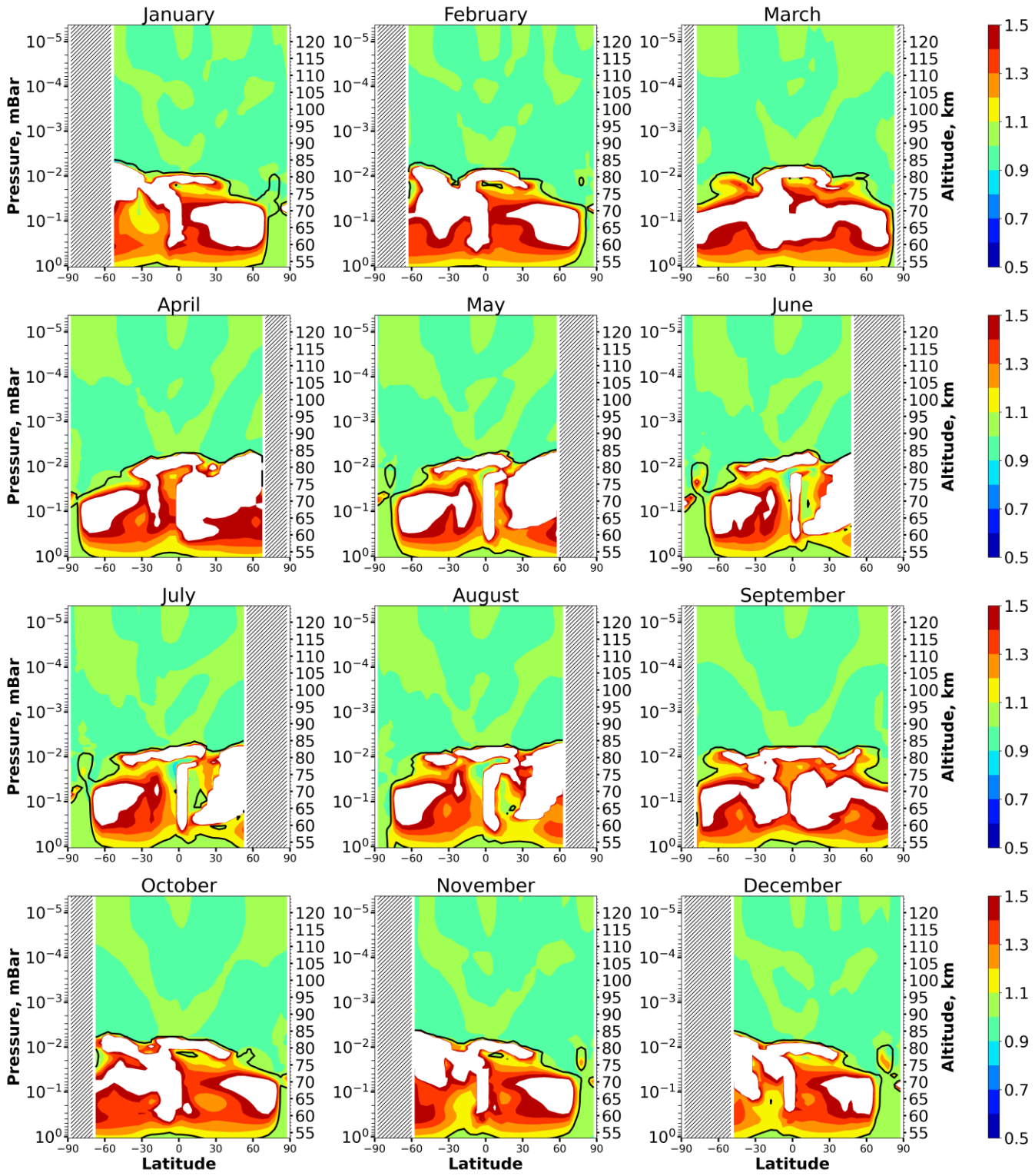

Figure 1. Nighttime mean and monthly averaged $HO_2/{HO_2}^{eq}$, where ${HO_2}^{eq}$ is equilibrium concentration determined by Eq. (5). Black line shows the boundary of HO_2 equilibrium according to condition (1). The stippling corresponds to χ<105°. The white area represents the $< HO_2/{HO_2}^{eq} >$ ratio outside the [0.5, 1.5] interval.

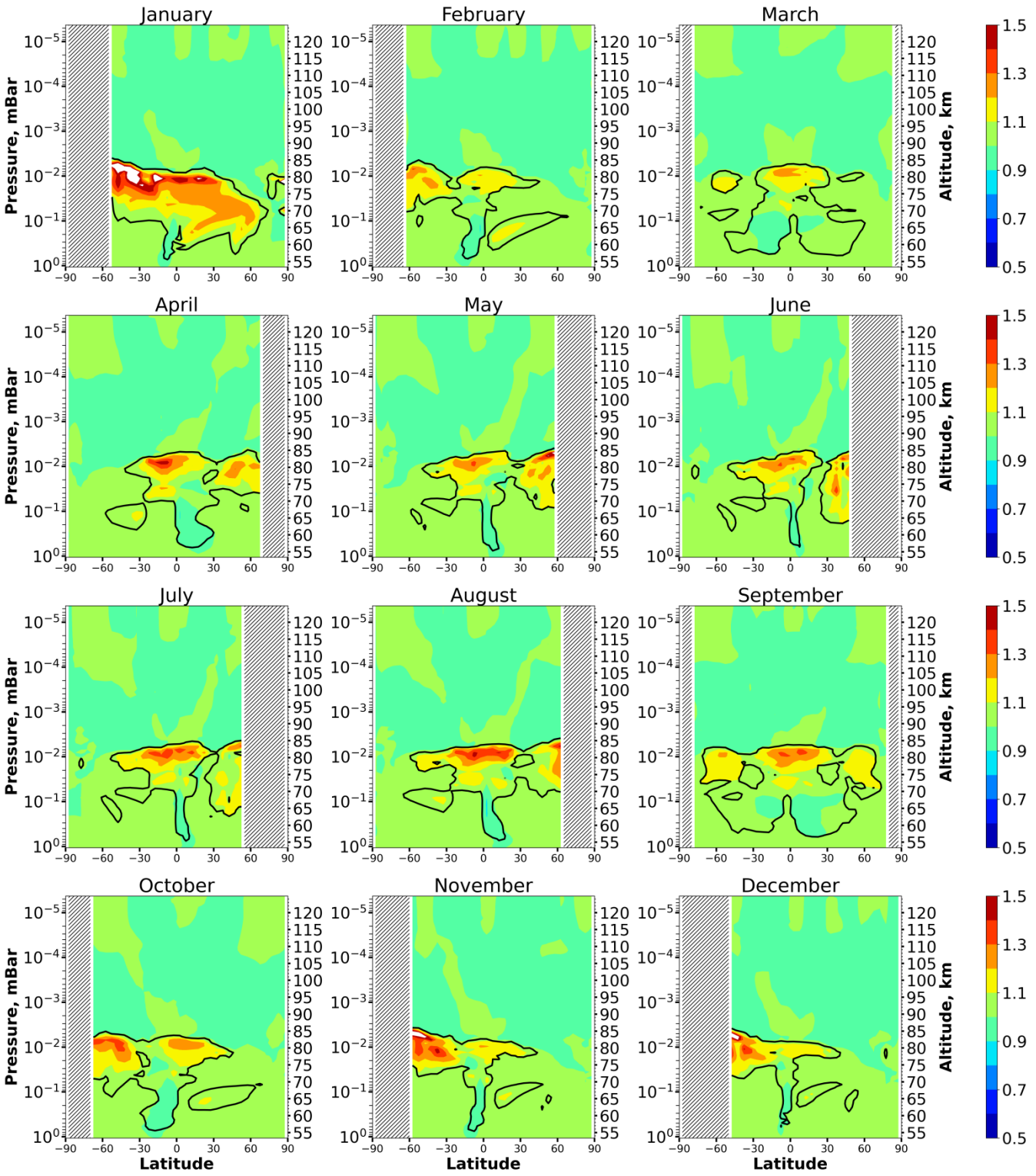

Figure 2. Nighttime mean and monthly averaged OH/OH^{eq}, where OH^{eq} is equilibrium concentration determined by Eq. (6). Black line shows the boundary of OH equilibrium according to condition (1). The stippling corresponds to χ<105°. The white area represents the $< OH/OH^{eq} >$ ratio outside the [0.5, 1.5] interval.

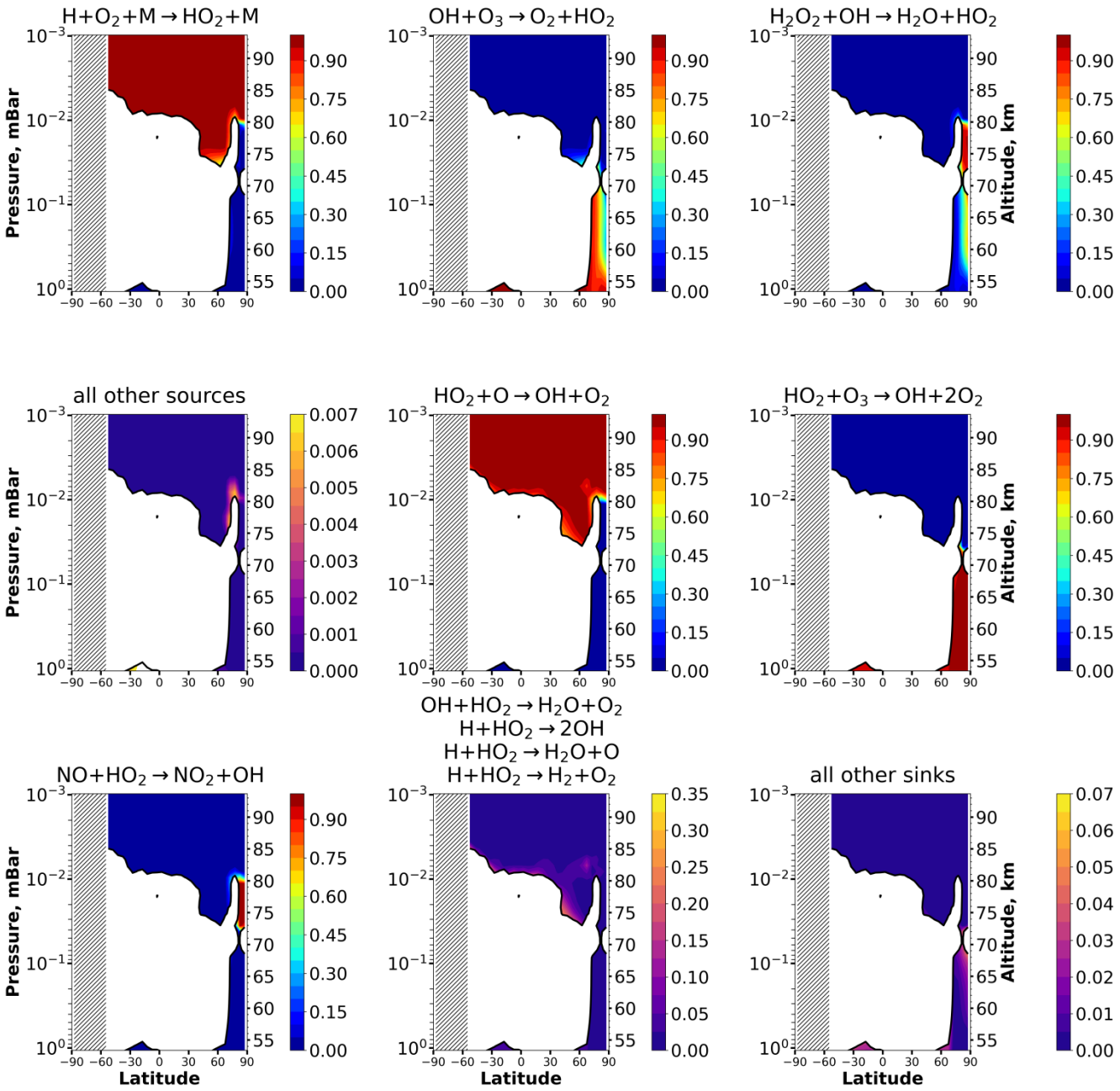

Figure 3. Nighttime mean and monthly averaged relative contribution of a certain reaction to the total source or sink of HO_2 in equilibrium areas. The stippling corresponds to χ<105°. White color indicates nonequilibrium areas of HO_2.

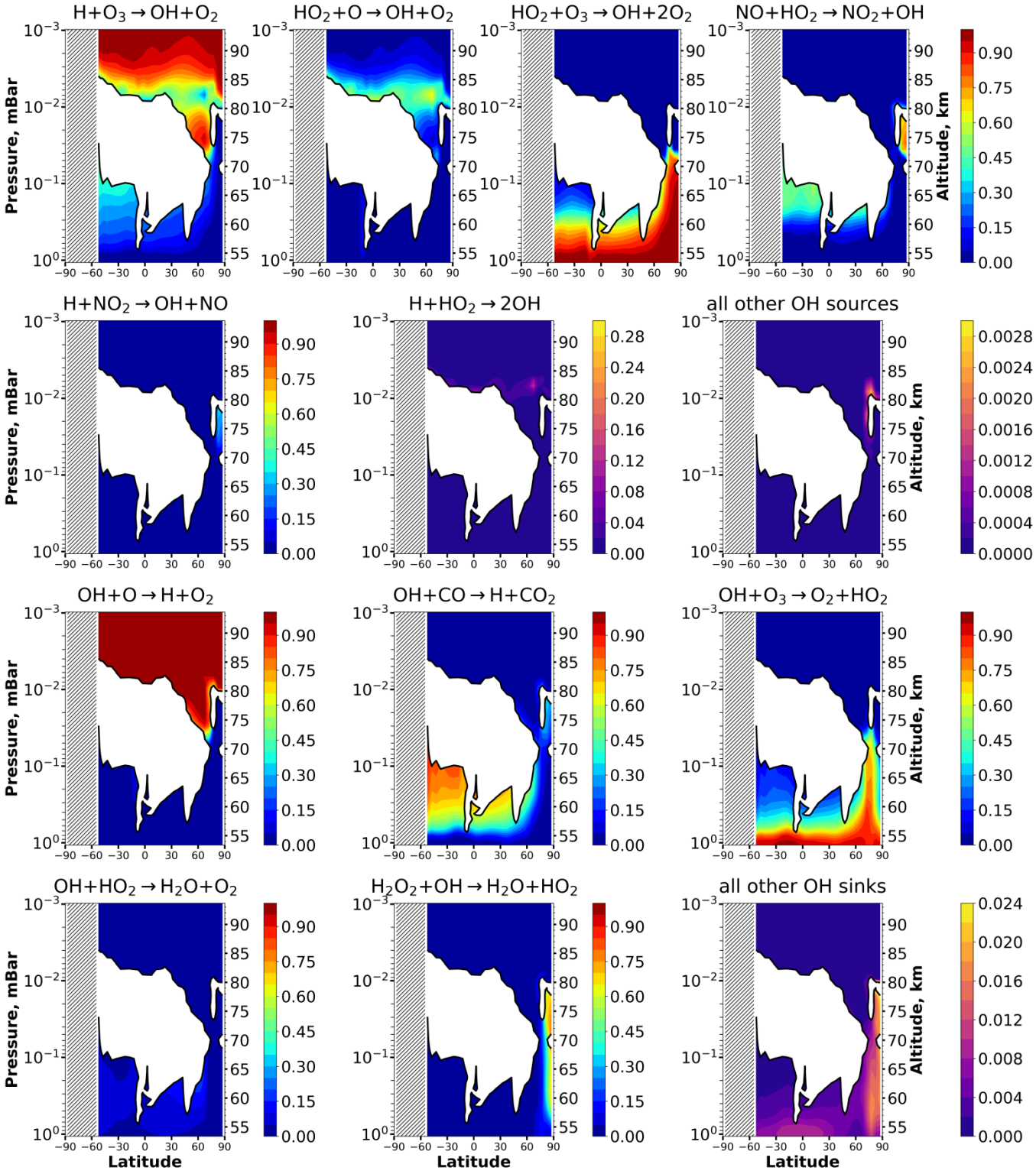

Figure 4. Nighttime mean and monthly averaged relative contribution of a certain reaction to the total source or sink of OH in equilibrium areas. The stippling corresponds to χ<105°. White color indicates nonequilibrium areas of OH.

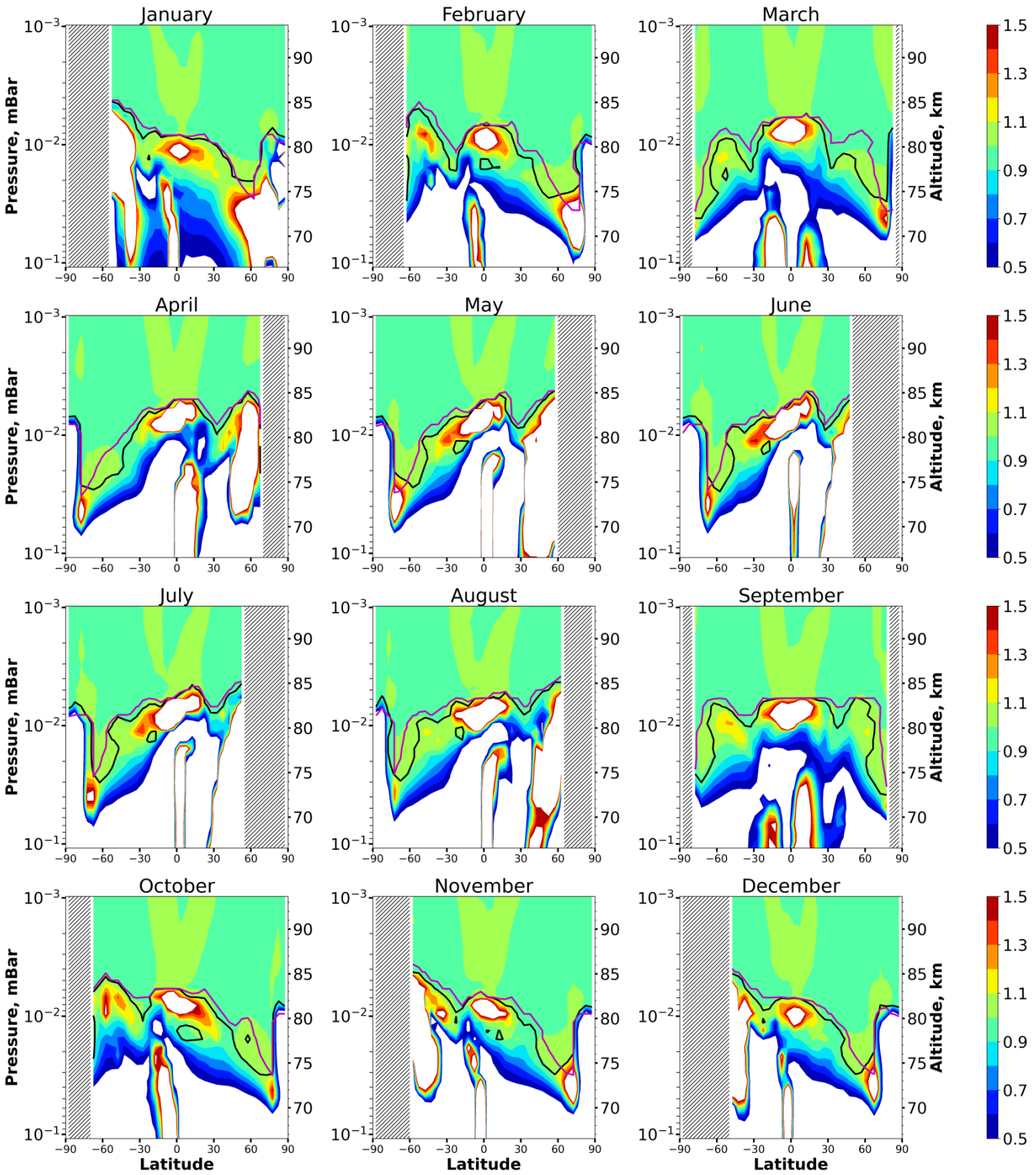

Figure 5. Nighttime mean and monthly averaged $HO_2/HO_{2_{sh}}^{eq}$, where $HO_{2_{sh}}^{eq}$ is shortened equilibrium concentration determined by Eq. (9). Black line shows the boundary of HO_2 equilibrium according to condition (1). Magenta line shows $< Crit_{HO_2} >= 0.1$. The stippling corresponds to χ<105°. The white area represents the $< HO_2/HO_2{}^{eq} >$ ratio outside the [0.5, 1.5] interval.

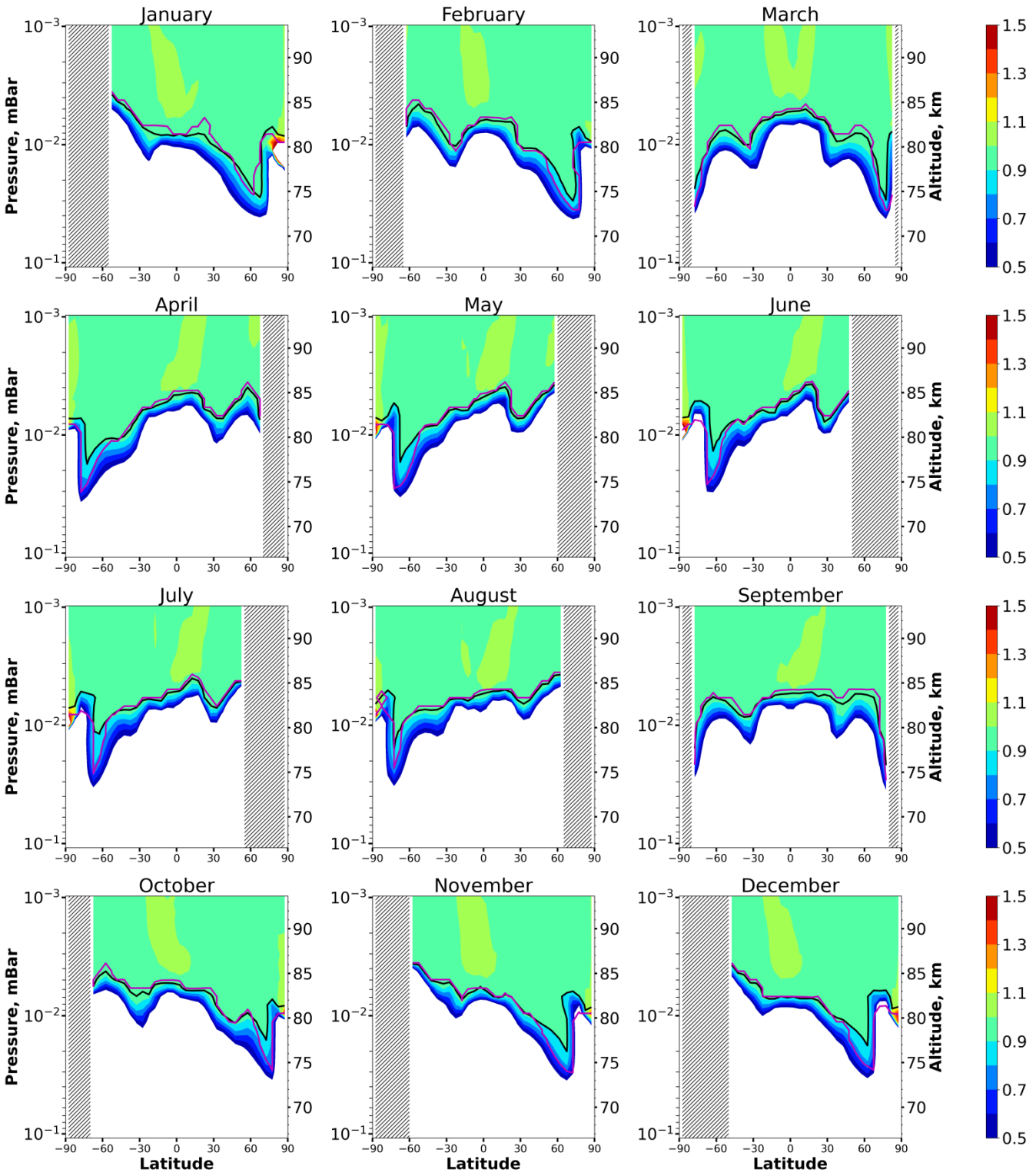

Figure 6. Nighttime mean and monthly averaged OH/OH_{sh}^{eq}, where OH_{sh}^{eq} is shortened equilibrium concentration determined by Eq. (10). Black line shows the boundary of OH equilibrium according to condition (1). Magenta line shows $< Crit_{OH} >= 0.1$. The stippling corresponds to χ<105°. The white area represents the $< OH/OH^{eq} >$ ratio outside the [0.5, 1.5] interval.

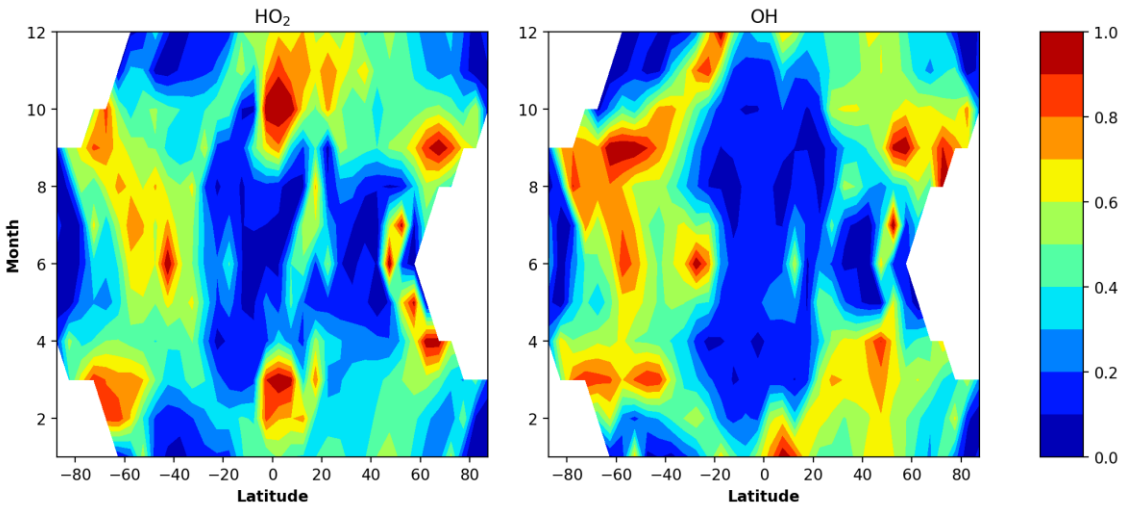

~~Figure 7.~~

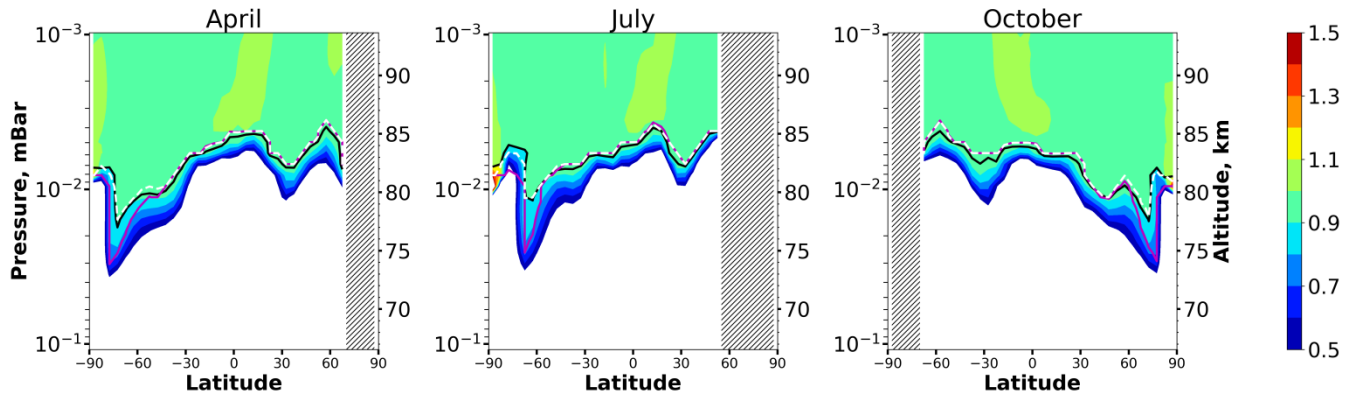

Figure 7. Nighttime mean and monthly averaged OH/OH_{sh}^{eq}. Black line shows the boundary of OH equilibrium according to condition (1). Magenta line shows $< Crit_{OH} >= 0.1$, dotted white line shows $< Crit_{OH}{}^{m} >= 0.1$.

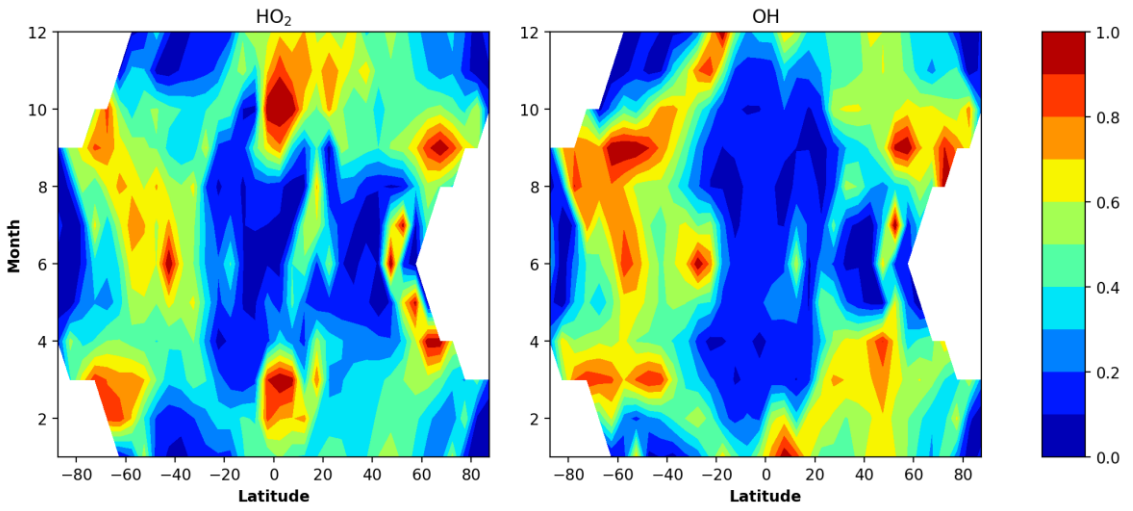

Figure 8. Monthly and longitudinally mean of total uncertainties in determination of the local heights of the OH and HO_2 equilibrium boundaries according to the criteria (17) and (25). The white color indicates the absence of data due to polar day.

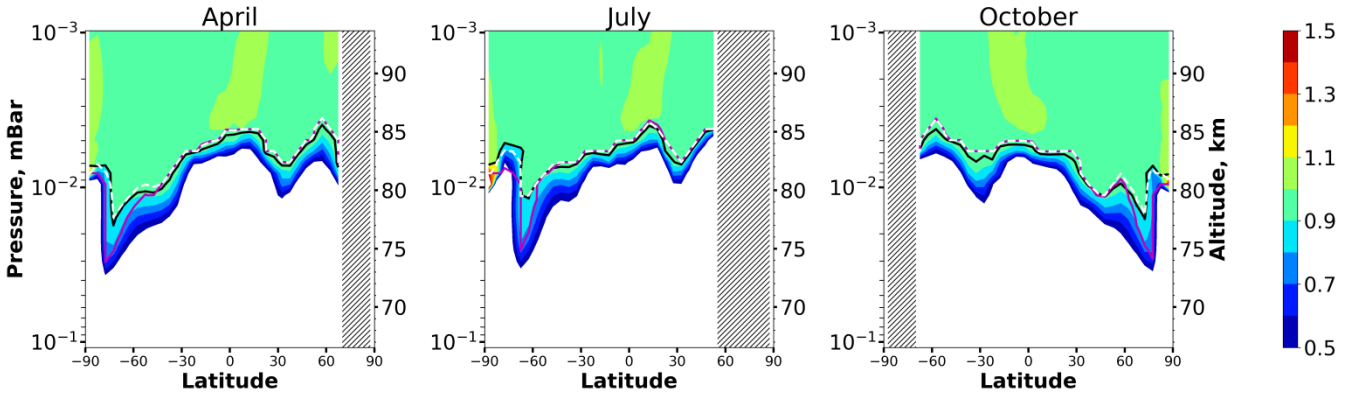

~~Figure 8. Nighttime mean and monthly averaged OH/OH_{sh}^{eq}. Black line shows the boundary of OH equilibrium according to condition (1). Magenta line shows $< Crit_{OH} >= 0.1$, dotted white line shows $< Crit_{OH}^{**} >= 0.1$.~~